Quantifying sediment mass redistribution from joint time-lapse gravimetry and photogrammetry surveys

Maxime Mouyen[1], Philippe Steer[2], Kuo-Jen Chang[3], Nicolas Le Moigne[4], Cheinway Hwang[5], Wen-Chi Hsieh[6], Louise Jeandet[2], Laurent Longuevergne[2], Ching-Chung Cheng[5], Jean-Paul Boy[7], Frédéric Masson[7].

[1]Department of Earth and Space Sciences, Chalmers University of Technology, Onsala Space Observatory, SE-439 92 Onsala, Sweden.
[2]Univ Rennes, CNRS, Géosciences Rennes, UMR 6118, 35000 Rennes, France.
[3]Department of Civil Engineering, National Taipei University of Technology, Taipei 10608, Taiwan, R.O.C.
[4]Géosciences Montpellier, UMR CNRS/UM2 5243, Université Montpellier 2, CNRS, Montpellier, France
[5]Department of Civil Engineering, National Chiao Tung University, Hsinchu 300, Taiwan, R.O.C.
[6]Industrial Technology Research Institute, Hsinchu 310, Taiwan, R.O.C.
[7]Institut de Physique du Globe de Strasbourg, CNRS - Université de Strasbourg UMR 7516 - Ecole et Observatoire des Sciences de la Terre, 67084 Strasbourg Cedex, France.

Correspondence to: Maxime Mouyen (maxime.mouyen@chalmers.se)

Abstract. The accurate quantification of sediment mass redistribution is central to the study of surface processes, yet it remains a challenging task. Here we test a new combination of terrestrial gravity and drone photogrammetry methods to quantify sediment mass redistribution over a 1-km^2 area. Gravity and photogrammetry are complementary methods. Indeed, gravity changes are sensitive to mass changes and to their location. Thus, by using photogrammetry data to constrain this location, the sediment mass can be properly estimated from the gravity data. We carried out 3 joint gravity-photogrammetry surveys, once a year in 2015, 2016 and 2017 over a 1-km^2 area in southern Taiwan featuring both a wide meander of the Laonong River and a slow landslide. We first removed the gravity changes from non-sediment effects, such as tides, groundwater, surface displacements and air pressure variations. Then, we inverted the density of the sediment, with an attempt to distinguish the density of the landslide from the density of the river sediments. We eventually estimate an average loss of $3.7 \pm 0.4 \times 10^9$ kg of sediment from 2015 to 2017, mostly due to the slow landslide. Although the gravity devices used in this study are expensive and need week-long surveys, new instrumentation progresses shall enable dense and continuous measurements at lower cost, making this method relevant to improve the estimation of erosion, sediment transfer and deposition in landscapes.

1 Introduction

The reliable quantification of sediment mass redistribution is critical to the understanding of surface processes (Dadson et al., 2003; Hovius et al., 2011; Morera et al., 2017) and has significant implications for studies in tectonics (Molnar et al., 2007; Steer et al., 2014; Willett, 1999), climate (Peizhen et al., 2001; Steer et al., 2012), human activities (Horton et al., 2017; Torres et al., 2017) or biochemistry (Darby et al., 2016). Areas with rapidly changing landscapes are ideal places to quantify local

erosion and sedimentation processes. Optical methods such as light detection and ranging (LIDAR) and photogrammetry, which accurately measure surface elevation, allow to compute changes of sediment volumes at timescales that are compatible

35 with nearly live observations (Jaboyedoff et al., 2012). These timescales range from a few seconds for a landslide to a few years for the evacuation of the collapsed materials by rivers (Croissant et al., 2017; Hovius et al., 2011). The sediment volumes must then be converted into masses before being assimilated into either surface process models, which are governed by mass conservation equation of sediment, or into sediment redistribution variables, such as entrainment, sediment load or sediment delivery, which all refer to sediment mass (Aksoy and Kavvas, 2005; Ferro and Porto, 2000; Milliman and Farnsworth, 2011).

40 Converting volumes to mass requires an independent measure of local values of the bulk density of sediments or rocks. Such in situ measurements are time-consuming and may not capture the local heterogeneity of the redistributed materials. Therefore, we develop here a new approach, combining photogrammetry and terrestrial time-lapse gravimetry to estimate average sediment densities over the investigated area and to convert the volume of redistributed sediment into a mass. The interest of gravimetry is that it directly senses all mass changes around the measurement site. This combined approach returns a density

45 that automatically averages all sediment density heterogeneities of the area without the need for dense in situ density measurements. The fact that gravimetry requires good constraints on the localisation of mass changes is solved by the photogrammetry measurements. In this study, we quantify the sediment mass redistribution over an area of ~1 km^2 in southern Taiwan (Fig. 1), between 2015 and 2017. It aims at complementing suspended sediment measurements to better assess sediment mass redistribution at decadal timescales. The studied area hosts both a slow landslide and a river carrying sediments

50 eroded from the inner part of the mountainous catchment.

Time-lapse gravimetry, that is the measure of gravity changes with time at a fixed location, is the only geophysical tool directly sensitive to mass redistributions at and below the earth's surface. It has been widely applied in the fields of glaciology, hydrology and solid earth processes, either from space, with the Gravity Recovery and Climate Experiment (GRACE) mission

55 (Farinotti et al., 2015; Han et al., 2006; Longuevergne et al., 2013; Pail et al., 2015; Tapley et al., 2004), or from terrestrial instruments (Van Camp et al., 2017; Crossley et al., 2013). Recent studies demonstrate the new potential of time-lapse gravity for studying surface processes as well, because the mass of deposited or eroded sediment can also significantly alter the gravity field (Liu et al., 2016; Mouyen et al., 2013, 2018). Since gravimetry is presently undergoing a revival thanks to recent technological progresses (Ménoret et al., 2018; Middlemiss et al., 2016, 2017), new ranges of applications such as sediment

60 mass quantification shall be encouraged to promote the use of gravimetry outside the field of geodesy.

The classical limitation for gravimetry is the non-uniqueness of its solutions, since gravity changes are integrative and sensitive to both mass variations and to the location where these mass variations take place (Fig. 2 and equation 1). Nevertheless, network gravity surveys have showed their high value to estimate below ground mass changes in hydrology (Jacob et al., 2010;

65 Naujoks et al., n.d.), volcanology (Carbone and Greco, 2007; Kazama et al., 2015) or reservoir monitoring evolution (Ferguson et al., 2008; Hare et al., 2008). When studying underground processes, especially groundwater, it is common to simplify the

redistribution to a one-dimension problem. The groundwater level variations Δh are the main observable and gravity effects are computed using a Bouguer plate ($2\pi G \rho_{water} \Delta h$). This simplification is necessary because it is usually impossible to monitor lateral groundwater redistribution, yet it remains appropriate for homogeneous aquifers. The groundwater level

70 variation can be assumed constant over the entire aquifer. Such an assumption is not valid for surface processes because sediment build complex three-dimensional bodies. But sediment mass redistributions occur at the ground's surface, thus, they are accessible to accurate location methods such as photogrammetry (Eltner et al., 2016; Niethammer et al., 2012; Schwab et al., 2008). Combining accurate geometries with gravity variations must thus enable proper mass estimations. Fig. 2 illustrates the use of time-variable gravimetry to quantify sediment mass redistribution at the earth's surface. In the simplest case, when

75 considering each ground element as a point-mass, the total change of gravity $\varDelta g$ measured between t_0 and t_1 is:

$$\Delta g = g_{t1} - g_{t0} = \sum_{i=1}^{N} \Delta g_i = \sum_{i=1}^{N} \frac{Gm_i}{r_i^2} sin\theta \qquad (1)$$

where $\varDelta g_i$ is the vertical component of the gravitational change at each element i (i ranging from 1 to N = 28 in Fig. 2b) considered as a point-mass (Fig. 2c) of mass m_i located at a distance r_i from the gravimeter, and G is the universal gravitational constant. Note that the gravitational attraction of any element decreases with the square of the distance between this element

80 and the site where gravity is measured, so that the distance of the mass redistribution can be a strong limiting factor to measure significant gravity changes. Note also how the angle θ between the point mass and the site where gravity is measured contributes to the gravity effect. The gravity effect is maximum when the point mass is at the vertical of the site, negative if above the site, positive if below. If the point mass is exactly at the horizontal with the gravimeter sensor, then the gravity effect cancels. The effects of the angle and the distance are shown in Fig. 2d and 2e, for a general case and for one actual site of the

85 survey, respectively. Point-mass simplification is ideal to grasp the concept of gravimetry but it is not suitable for precise quantifications aimed to in this study. All gravity modelling will thus be done using rectangular prism modelling (Nagy, 1966), which is the most appropriate way to compute the gravity effect of surface changes measured by photogrammetry.

After introducing the study area, we describe the gravimetry and photogrammetry surveys that we conducted, together with

90 our data processing workflow. We then show the results of both methods and interpret them jointly in order to retrieve the mass of sediment redistributed in this area from 2015 to 2017. We eventually discuss the benefits and limits of this method.

2 Study area

The joined gravimetry-photogrammetry survey was set in southern Taiwan, at the Paolai village, next to the Laonong River (Fig. 1). The gravity network contains one site, AG06, for absolute gravity (AG) measurement and nine sites, BA01 to BA09,

95 for relative gravity (RG) measurements. During the 2017 survey, all sites but BA02 were located to cm accuracy using Global Navigation Satellite System (GNSS) enhanced by real-time kinematic (RTK) technique. The exact location of BA02 could not be measured due to the unexpected storage of concrete blocks, referred to as dolosse, aiming at being placed on the river shore

to protect it from erosion. This dolosse storage also covered BA03 and BA04 but those two sites could still be measured. The gravimetric effect of the dolosse was estimated and removed from the measurements.

100

The first reason for choosing this location is that time-lapse absolute gravity surveys have been done at AG06 since 2006, in the frame of the Absolute Gravity in the Taiwan Orogen (AGTO) project. This project permitted to measure, for the first time, sediment mass redistribution using time-lapse absolute gravimetry and shown that significant sediment transfers occurred around Paolai (Kao et al., 2017; Mouyen et al., 2013). Indeed, this site experiences vigorous sediment transfer processes

105   powered by heavy rains brought by tropical cyclones (typhoons) and monsoonal events, especially in May to August (Chen and Chen, 2003). The heavy rains destabilize the slopes of the Taiwanese high mountains, triggering landslides and debris flows (Chiang and Chang, 2011). This occurs on a regular basis: 5 to 6 typhoons make landfall in Taiwan every year (Tu et al., 2009), mostly between May and September. The most remarkable event was the 2009 Morakot typhoon, which produced the worst flooding in the last 60 years in Taiwan and up to 2777 mm of accumulated rainfall (Ge et al., 2010) and triggered 22

110   705 landslides with a total area of 274 km^2 (Lin et al., 2011). Landsliding, which can also be triggered by regional active tectonics, is the main process supplying sediment to rivers in Taiwan (Dadson et al., 2003; Hovius et al., 2000).

The second reason for choosing this location is practical. Indeed, this location offers a stabilized path made of concrete on the southern bank of the Laonong River, where the relative gravity benchmarks could be properly set, on stable and sustainable

115   sites, and easily accessed for measurements. Also, a continuous GNSS station, PAOL (latitude: 23.10862°, longitude: 120.70287°, elevation: 431 m), is co-located with the AG06 pillar and is maintained by the Institute of Earth Sciences-Academia Sinica (IES-AS, 2015). This permits to precisely take into account gravity changes only due to ground vertical displacements.

120   In this area, both the Laonong River and the landslide (Fig. 1) are susceptible to sediment transfers. The gravimetry-photogrammetry survey is setup to focus on these processes. Note that what we call the river (plain black line contour in Fig. 1) is the active channel bed that includes emerged alluviums. During yearly measurements, the water extent of the river only covers a fraction of this area, even if the period 2015-2017 has seen some higher water level and larger extents, especially during large floods.

125   **3 Methods**

This section introduces the two main methods used in this study: gravimetry and photogrammetry. Gravimetry is sensitive to masses and their distribution, while photogrammetry is here a geometric measure of the ground surface, hence of the sediment distribution. Therefore, combining gravimetry and photogrammetry removes the geometric ambiguity inherent to gravity

measurements and allows to focus on sediment masses. This combination is done through a least-squares inversion to
130 determine sediment density, that is a mass per unit of volume.

3.1 Time variable gravimetry

Gravity was measured at 10 sites (Fig. 1) in 2015, 2016 and 2017, always over two days in November, since the climatic
conditions during this month are usually suitable for gravimetry fieldwork (e.g. no typhoon nor heavy rains, reasonable
temperatures). By measuring gravity during the same period of the year, we also expect to minimize hydrological effects,
135 which have an strong annual periodicity in this area (Chen and Chen, 2003). Absolute and relative gravity surveys were done
in parallel, the same days.

Relative gravity measurements were done using a Scintrex CG5 Autograv (serial number 167). The measurement principle is
to assess length variations of a spring holding a proof mass between different times and places, using a capacitive displacement
transducer, and convert them into gravity variations (Scintrex Ltd., 2010). The instrument is levelled at each site and repeats
140 90-seconds measurements continuously. We stop measurements when gravity readings repeat within 3 μGal (1 μGal = 10^{-8} m s^{-2}), while the internal sensor temperature remains stable. This usually takes 10 to 15 measurements, that is 15 to 23
minutes, although up to 25 measurements were required in some rare cases. Only the latest measurements, when gravity
readings are stable, are used in the gravity network adjustment, to estimate the drift. Indeed, relative gravimeter measurements
are subjected to an instrumental drift, which is corrected using the software Gravnet (Hwang et al., 2002). Inferring this drift
145 requires to re-measure one or more sites within a few hours. In this study, all surveys start and end at AG06, which is also re-
visited up to four times during the survey, together with other relative gravity sites (Appendix A). In addition, ambient
temperature alters gravity measurements at a rate of -0.5 Gal °C^{-1} (Fores et al., 2017). This effect was taken into account before
adjusting the instrumental drift of the gravimeter.

150 The absolute gravity measurements were done using a Micro-g FG5 (serial number 224), which monitors the drop of a free-
falling corner-cube in a vacuum. During its free fall, the positions and times of the corner-cube are precisely assessed using
laser interferometry and an atomic clock (Niebauer, 2015; Niebauer et al., 1995). One measurement takes ~12 hours and
consists in 24 sets of 100 test mass drops started every 30 min (one drop every 10 s). Measurements are always done overnight,
when anthropogenic seismic noise and temperature variations are lower than during day time. A laser problem in the FG5
155 prevented us from measuring absolute gravity in 2017. This is compromising since the measurements at BA01-BA09 need an
absolute reference to be compared with their previous survey in 2016. In order to proceed to the interpretation of the 2017
relative gravity survey, we decide to estimate the AG06 absolute gravity value in 2017 as the mean of the values measured in
2014, 2015 and 2016, that is 978 713 845.1 ± 3 μGal (Fig. 3). We believe this is a reasonable hypothesis because there were
no major climate or tectonic events between November 2016 and November 2017 around the Paolai region. In addition, by
160 repeating the gravity surveys at the same time of the year, in November, the gravity difference due to hydrological changes
are at the few-microgal level, which is about the size of the errors in the relative gravity measurements. The hydrological

conditions are described in more details in the next paragraphs. For this estimated absolute gravity value, we arbitrarily set the standard deviation to a value about three times larger than usual at this site. The AG06 values in 2016 and 2017 are quite similar, less than 0.5 µGal difference. Although absolute gravity measurements at AG06 started in 2006 and repeated once a

165   year except from 2011 to 2013, it is not possible to use these older data for the estimation of the 2017 value. Indeed, in 2009, typhoon Morakot and its subsequent massive landslides reset the whole area. The gravity offset between November 2008 and November 2009, i.e. before and after Morakot, is about 30 µGal and is due to large sediment redistribution in this area (Mouyen et al., 2013). Sediment redistribution due to Morakot was such an exceptional event, with a significant impact on gravity, that it must not be included in the extrapolation of the 2017 gravity value. The measurements from 2009-2010 were not used either

170   because too much reconstruction work was ongoing at that time, taking out debris from the river, thus interfering with natural sediment redistribution.

To focus on sediment mass redistribution, other sources responsible for gravity changes must be removed from the gravity time series. Here, these effects are the tides, air pressure variations, polar motions, vertical ground motions and hydrology.

175   These corrections are detailed in the next paragraph and summarized in Table 1.

Solid earth tides are computed using TSOFT (Van Camp and Vauterin, 2005) using tidal parameters from Dehant *et al.* (1999), referred to as WDD. Ocean tide loading effects are computed using the FES2004 model (Letellier et al., 2004) with the Ocean Tide Loading provider (Bos and Scherneck, 2003). Polar motions effects are computed using the International Earth Rotation and Reference System Services parameters and the Absolute Observations Data Processing Standards (Boedecker, 1991).

180   Atmospheric effects, that is gravity changes due to air masses, are corrected using local barometric records done at a continuous weather station located ~12 km west of Paolai (station C0V250) and an admittance factor of -0.3 µGal hPa^{-1} (Merriam, 1992). Solid Earth tides, ocean tide loading and atmosphere loading are corrected before the drift adjustment of the relative gravity measurements, because they can have significant effects over a few hours, that is while the relative gravity survey is done. Not correcting them would bias the drift estimation by mixing gravity changes due to the instrumental drift with those due to tides

185   and atmosphere. Vertical displacements of the ground also change the gravity, because the gravity measured at any place on the Earth's surface depends on the inverse of the square of the distance between this site and the Earth's center of mass. Therefore, if the site is uplifting (further from center of mass) or subsiding (closer to the center of mass), it will have a lower or higher gravity value, respectively. This effect is corrected using continuous GNSS time series recorded at AG06 (the GNSS site PAOL is co-located to AG06, Fig. 4) and assuming a theoretical ratio $\Delta g/\Delta z = -2$ µGal/cm (Van Camp et al., 2011), where

190   Δg is the gravity change and Δz is the elevation change, at the same location. Between 2015 and 2017, the ground uplift at AG06 is about 1.3 cm yr^{-1}. That is a large uplift rate, explained by the active mountain building processes at work in Taiwan, where up to 1.9 cm.yr^{-1} uplift is measured (Ching et al., 2011). Although the relative gravity sites are between 300 and 500 m from the PAOL permanent GNSS, we apply the same uplift correction to these sites as to AG06. Indeed, tectonic uplift is a regional feature and can be assumed constant over a few hundred meters, unless an active fault or more cross the area. But

195   there is no evidence for such a fault in Paolai.

We also correct the effect of hydrology, which deforms the earth surface at the global scale and changes the groundwater mass attraction at local scales, near the gravimeter. This correction relies on global hydrological models. We consider two of them in this study:

200
1. the Global Land Data Assimilation System Version 2 (GLDAS-2) forcing the Noah land surface model (Rodell et al., 2004) and

2. the Modern-Era Retrospective Analysis for Research and Applications, version 2 (MERRA-2, Gelaro et al., 2017).

The gravitational effect due to each of these models is provided by the EOST loading service (Boy, 2015; Petrov and Boy, 2004). Unlike the other corrections, the hydrological correction may suffer large uncertainties because of (1) the complexity

205 of hydrological processes, (2) the difficulty to measure groundwater and (3) its large effect on gravity (Jacob et al., 2009; Longuevergne et al., 2009; Pfeffer et al., 2013). Indeed, the effect of GLDAS-2 and MERRA-2 on gravity predict up to 20 μGal of seasonal amplitude in the hydrological signal, with sometimes large differences, up to 10 μGal, between the different models (Fig. 5). Nevertheless, surveying in November appears as a valuable way to decrease the hydrological impact on the gravity data, since this effect is lower than 3 μGal, with any of the two hydrological models. Eventually we use the average

210 hydrological effect from GLADS-2 and MERRA-2. We arbitrarily set an uncertainty of 5 μGal to this correction (Table 1), to account for possible bias in the models.

We also correct the effect of the dolosse set in 2017, which is only significant at BA03 and BA04. These structures, located above BA03 and BA04, were ~~indeed~~ responsible for an artificial decrease of gravity of about 15 μGal. Their gravitational

215 effect is computed using the dolosse's geometry measured by the photogrammetry and rectangular prism method (computation details in Appendix B). Given the uncertainty of this correction process, we add an arbitrary 5 μGal uncertainty on the gravity changes measured at BA03 and BA04 during the 2017 survey.

The last non-sediment effect on gravity is the actual Laonong River: water with density $\rho_w = 10^3$ kg m^{-3}. The photogrammetry

220 ~~actually~~ measures the river surface but not its depth. Also, at each survey, the river did not follow the same path across the active river bed. Therefore, neither the volume of the river nor its variation can be estimated, which prevents us from a gravity correction for the river.

3.2 Photogrammetry

The purpose of the photogrammetry survey is to generate high resolution digital surface models (DSM) in 2015, 2016 and

225 2017, at the moment of the gravity surveys, to quantify the sediment volumes changes between each survey.

3.2.1 Equipment

The photogrammetry survey was done with an unmanned aerial vehicle (UAV), commonly known as a drone, which is commonly used in morphotectonics studies (Chang et al., 2018; Deffontaines et al., 2017, 2018). The UAV is a modified already-available Skywalker X8 fixed-wing aircraft reinforced by carbon fiber rods and Kevlar fiber sheets (Figs. 6a and 6b). To generate a high-resolution DSM, orthorectified mosaic images, and a true 3D model, the UAV is equipped with a Sony ILCE-QX1 global shutter camera and a 16 mm SEL16F2.8 lens.

3.2.2 Survey design and execution

The UAV is launched by hand, then flies, takes photos, and lands autonomously by using a pre-programmed flight plan. The autopilot system is composed and modified from the open source APM (Ardupilot Mega 2.6 autopilot) firmware and open source software Mission Planner (Oborne, 2010), transmitted by ground-air XBee radio telemetry.

The UAV was flown between 300 and 500 m above the ground level. It covered an area of about 15-20 km^2 with about 15-20 cm ground sampling distance (GSD) in one single flight mission (Table 2). Repeated adjacent photographs were kept for at least 85 % endlap and 50 % sidelap. The GPS location of the acquired image is recorded on the auto-pilot log. Each UAV flight missions took about 90 min. On average 13 ground control points (GCP) per survey and 11 check points (CKP) were measured in the field to control and verify the quality of the datasets (Fig. 6c). The GCP are pre-existing or painted benchmarks on the ground. The CKP are permanent features such as bricks with patterns, road sign and zebra crossing. The GCP and CKP coordinates were measured by Virtual Base Station (VBS) RTK GPS and RTK GPS at least 3 times each. The mean vertical error and the root mean square are 1.5 cm and 4.2 cm, respectively.

3.2.3 Photogrammetry processing and results

The images acquired by the UAV, their positions and the GCP positions are processed using Pix4Dmapper (Pix4D, 2020) in order to generate a DSM, with a grid spacing of 50 cm based on multi-view stereo, which aims at reconstructing a complete 3D object model from a collection of images taken from known camera viewpoints (Furukawa and Ponce, 2010; Seitz et al., 2006). Images and camera parameters such as focal length, principal point, radial distortion, tangential distortion, aspect ratio and skew are auto-adjusted for each image during the processing. The point cloud densification and DSM parameters set specifically for Pix4Dmapper are summarized in Table 3.

The quality of the DSM is calculated by comparing its elevation with those of the CKP at the same coordinates. The error of the dataset is denoted as Table 4, where the data shows that the mean of the error compared with field survey about 0.11-0.20 m and with standard deviation of 0.334 to 0.622 m.

4 Survey results

The results of the gravity and photogrammetric surveys are summarized in Figs. 7 and Table 5. The largest gravity changes occurred between 2015 and 2016, with most sites showing an increase of more than 30 µGal. On the contrary, the gravity decreased at most sites from 2016 to 2017. When measured above the redistributed masses, increase and decrease of gravity correspond to gain and loss of masses, respectively. Qualitatively, this is in agreement with the corresponding digital surface models (DSM) changes in the active bed channel showing higher sediment thicknesses, thus a gain of mass, from 2015 to 2016 and large surfaces of lower sediment thicknesses from 2016 to 2017. Over the time period 2015-2016, the top of the landslide is actively eroded, up to 46 m, while its toe displays significant sedimentation, up to 33 m. The active river bed shows a mixed-pattern of erosion and sedimentation, between -1.19 and 1.21 m on average, possibly resulting from the migration of the river braids. Whereas, over the time period 2016-2017, the landslide displays mostly erosion, up to 39 m, while the river bed continues to display a mixed-pattern of erosion and sedimentation, between -1.17 and 1.08 m on average.

The gravimetric and photogrammetric techniques show large changes in gravity and topography, which demonstrate active processes of sediment mass redistribution in the river and on the slow landslide. In the next section, we combine these results to assess the mass of sediment redistributed from 2015 to 2017. Note that we focus the DSM analysis to the area bounded by the black line in Figs. 7d and 7e, which is restricted to the landsliding zone and the river.

5 Joint analyses of the gravity and photogrammetry data

Using the DSM, we build rectangular prisms with horizontal sides of 0.5 m, i.e. DSM resolution, and a vertical side as high as the elevation at the time of the corresponding surveys, i.e. bottom at 0 m and top at the surface elevation. Among the three (2015, 2016 and 2107) photogrammetric surveys, the 2017 survey has the smallest surface extent. Its limits are thus used to cut the 2015 and 2016 photogrammetric surveyed areas, so that all DSM cover the exact same area. The total mass of redistributed sediment equals the change of volume between each survey multiplied by the density of the sediment. We use the gravity data to assess this density using an inverse modelling approach. Note that since gravity decreases with the square of the distance between the measurement site and the mass location, we can bound our analysis to the area covered by the photogrammetric surveys without biasing the analysis. Indeed, using the wider 2015 and 2016 survey coverages, we find that extending our working area in the north-south and east-west directions by steps of 100 m does not alter the gravity changes computed at each sites by more than 1 %.

We design three inversion cases to retrieve the densities of the redistributed materials, using a least-square criterion. These cases are independent from each other and aim at increasing the amount of possibly different densities for comparison. Thus we invert:

- Case 1: The average density ρ of the material redistributed during the surveys.

- Case 2: The density of the sediment in the river ρ_r and the density ρ_l of the material in the landslide.
- Case 3: The density of the sediment in the river $\rho_r{}^{1615}$ from 2015 to 2016 and $\rho_r{}^{1716}$ from 2016 to 2017 and the density ρ_l of the material in the landslide.

Here we will solve an over-determined problem, where we have more observations (20 gravity differences over the three years) than variables to estimate (density, three at most, in case 3). However, gravity observations are too few and unevenly distributed over the study area to try to invert the density at each pixel (more than 4 millions) of the photogrammetry survey. In practice, the matrix representation of this system is (e.g. Hwang et al., 2002)

$$L + V = AX \tag{2}$$

where the design matrix $\mathbf{A}$, vector of unknowns $\mathbf{X}$ and vector of observations $\mathbf{L}$ are defined as

$$A = \begin{bmatrix} dg_{mod,r}^{1615,BA01} & 0 & dg_{mod,l}^{1615,BA01} \\ \vdots & \vdots & \vdots \\ dg_{mod,r}^{1615,AG06} & 0 & dg_{mod,l}^{1615,AG06} \\ 0 & dg_{mod,r}^{1716,BA01} & dg_{mod,l}^{1716,BA01} \\ \vdots & \vdots & \vdots \\ 0 & dg_{mod,r}^{1716,AG06} & dg_{mod,l}^{1716,AG06} \end{bmatrix} \tag{3}$$

$$X = \begin{bmatrix} \rho_r^{1615} \\ \rho_r^{1716} \\ \rho_l \end{bmatrix} \tag{4}$$

$$L = \begin{bmatrix} dg_{obs}^{1615,BA01} \\ \vdots \\ dg_{obs}^{1615,AG06} \\ dg_{obs}^{1716,BA01} \\ \vdots \\ dg_{obs}^{1716,AG06} \end{bmatrix} \tag{5}$$

and $\mathbf{V}$ is the vector of residuals ($\mathbf{X}$ and $\mathbf{V}$ are to be determined by the least-squares method). In matrices $\mathbf{A}$ and $\mathbf{L}$, dg is the gravity variation that is modelled (dg_{mod}) or observed (dg_{obs}) between 2016 and 2015 (1615) or between 2017 and 2016 (1716) at every site (BA01… AG06). The modelled gravity change can be computed for the material in river ($dg_{mod,r}$) or in the landsliding zone ($dg_{mod,l}$). This matrix representation is given for the inversion case 3 and can be simplified for cases 1 and 2.

The design matrix $\mathbf{A}$ is built thanks to the photogrammetry surveys, from which we identify the river and the landslides as well as their respective volume changes. Therefore, knowing also the position of the gravity sites, we compute each element of $\mathbf{A}$ using a gravity modelling by rectangular prisms methods (Nagy, 1966) and an arbitrary density equal to 1. The actual density can be inverted by

$$X = (A^T P A)^{-1} (A^T P L) \tag{6}$$

where $\mathbf{A}^T$ is the transpose of $\mathbf{A}$. The weight matrix $\mathbf{P}$ is diagonal, and its elements are the invert of the gravity uncertainties at each site i. The residuals $V = AX - L$ are used to compute a posteriori variance of the unit weight

$$\sigma_0^2 = V^T P V / (n - u) \tag{7}$$

where n is the number of gravity observations and u the number of unknown densities, and eventually the uncertainties of the inverted densities are the square root of the diagonal element of the a posteriori covariance matrix of **X**

320     $$C_X = \sigma_0^2 (A^T P A)^{-1} \tag{8}$$

The inverted densities for each case are summarized in Table 6. Cases 1 and 2 return similar densities. Case 3 returns a noticeable difference between the densities of the sediment in the active bed channel for the 2015/2016 or 2016/2017 surveys. A first hypothesis for this difference could be that the composition of the redistributed sediment has changed over the years of the study, for instance because they come from landslides that occurred in terrain with different densities. A second hypothesis

325   is that the water content of the sediment varies, eventually changing the effective density of the sediment as measured by the gravimeters. We do not have enough data to favour one of these hypothesis but we will discuss the possible influence of water on our density estimates in section 6.1. Uncertainties on the landsliding materials densities (case 2 and 3) are higher than those of the river sediment, likely because they are further from the gravity sites than the river sediment. As seen in equation 1, the further the redistributed masses are, the lower are their gravitational effects.

330

We described in section 3.1 the impossibility to remove the effect of the Laonong river (water) from gravity changes due only to sediment redistribution. As a workaround, here we simply assume a constant river depth of 1 m, which corresponds to rough field estimates. Then, we map the surface limits of the river from the optical images taken by the UAV during each survey. The height h of the river surface is given by the photogrammetry results. The river is then divided into prisms covering the

335   river area, with sides of 0.5 m, upper face at elevation h and lower face at elevation h-1, since the river is 1-m deep. We then compute the gravity effect of the river at each site of the network (except BA02, which position is unknown). This effect is removed from the gravity observation and the average density inversion (case 1) is run, giving $\rho = 1.7 \pm 0.1 \times 10^3$ kg m^{-3} and RMS = 9.7 µGal. This represents a decrease of 11% relative to the density $\rho = 1.9 \pm 0.1 \times 10^3$ kg m^{-3} given in Table 1 and also relative to the mass budget in Fig. 10. These values are yet to be taken with caution since we do not know the exact

340   geometry of the river, its depth in particular. In the rest of the study, we will only work with the density given in Table 1.

For comparison, during the 2017 survey, we evaluate the in situ densities of the materials in the active river bed and at the bottom of the landslide, at 22 sites (Fig. 8), also using photogrammetry (Appendix C). Estimating in situ density is time-consuming and demanding. It is done here only for comparison purposes; it is not required for the inversion. Indeed, joint

345   gravity-photogrammetry estimates an average in situ density over the surveyed area. Besides, in situ density measurements are done at discrete locations over an area made of heterogeneous material. The in situ densities range from 1.2 to 2.7×10^3 kg m^{-3} and are spatially heterogeneous, illustrating the variety of materials carried by the river and the landslide. Despite the limited and spatially uneven sampling points, we obtain an average density (2.0×10^3 kg m^{-3}) consistent with the average densities inverted from the gravity and photogrammetry data (1.9×10^3 kg m^{-3}). It is interesting to note that the density in the lobes of

350   the main, fresh, landslide (Fig. 8: the samples the most in the north, around 219500 m on the eastern axis) are among the lowest

density measured. These rocks in place, mostly slates, may have a higher density, about 2.7×10^3 kg m^{-3} (Ho, 1986). The landslide breaks them and stacked them into a rough, unorganized pile, less compact than the original material. As a result, using the average density of the rocks in this area would overestimate the mass.

355   The final comparison of the measured gravity and the computed gravity in cases 1, 2 and 3 is given in Fig. 9. The largest misfits are at BA05 and BA06 during the 2016-2017 period, for which gravity changes are underestimated by 19 and 15 μGal, respectively. Possible explanations for these two misfits are: a wrong site location, an error in the gravity data, an error in the DSM data or local but large hydrological effects, not accessible at the scale of the global hydrological models we used. However, we could not narrow our search down a specific issue at BA05 and BA06. At the other sites, the pattern and amplitude

360   of the gravity observations is rather well explained by the modelling. Note that in Fig. 9b, the gravity modelled at most sites seems to need a small offset of -3 μGals to fit within the error bars of the observations. This may show that our absolute gravity estimate for the 2017 survey (Fig. 3) is wrong by 3 μGals.

365   Multiplying the inverted densities (Table 6) with the volumes changes computed from the DSM changes, we can eventually compute the mass of sediment that were redistributed between two surveys, for each inversion cases (Fig. 10). Since the inverted densities are similar in each case (Table 6) and the volumes changes estimated from photogrammetry are identical, thus the estimated masses (volumes times density) are also similar in each three case. The difference mostly lies within the uncertainty of these estimates. In our mass estimation, we also differentiate the top and the toe of the landslide, because the top of the landslide mostly experience erosion, while its toe undergoes both erosion and sedimentation processes. This helps

370   to unravel how the sedimentation and erosion processes are distributed over the slow landslide.

    In the river only, we observe that the mass of sediment redistributed between each survey is similar. The river gained between 0.61 and 0.83×10^9 kg and lost between 0.58 and 0.74×10^9 kg. Thus, the mass loss is about 4% and 12% less than the mass gain, resulting in a quasi-balanced budget that is within the uncertainty of the mass estimations. The time variability of the

375   sediment mass budget is dominated by the landslide, which causes larger mass redistributions (up to 4×10^9 kg) and loss-to-gain ratios. A significant mass loss occurred between 2016 and 2017, which is ~15 times larger than the mass gain. Between 2015 and 2016, both erosion and sedimentation are significant at about 2 to 3×10^9 kg, which are rather balanced. A likely hypothesis is that we mainly observe a transfer of sediment from the top of the landslide, where $2.1 \pm 0.4\times10^9$ kg of material were eroded toward its toe, where $1.9 \pm 0.4\times10^9$ kg accumulated (average mass from the three cases). Overall, from 2015 to

380   2017, the area has lost about $3.7 \pm 0.4\times10^9$ kg of sediment. Note that this landslide occurs over several years, not in one quick event, probably as the consequence of the erosion by the meandering Laonong River.

6 Discussion

6.1 Implications for sediment transfers in active landscapes

Our results highlight how landscapes react to landsliding and how they evolve after a large perturbation such as the 2009
Morakot typhoon. Between 2015 and 2016, the activity of the Paolai slow landslide mostly consists in transferring about
2×10^9 kg (about 1×10^6 m^3) of materials form the landslide top to the landslide toe over roughly 100 to 200 m. After 2016, a
significant event of erosion of the landslide occurs, with more than 3×10^9 kg of sediment removed, including most of the
sediment previously deposited on the landslide toe. This corresponds to a particularly rapid evacuation of the sediment,
especially in the alluvial context of the Laonong river, that is yet consistent with predictions obtained with a morphodynamic
model by Croissant et al. (2017) for bedrock rivers. It is likely that the position of the landslide in the outer bank of a meander
has favoured sediment export efficiency. Despite this landslide activity, it is quite remarkable that the Laonong river roughly
maintains a neutral sediment budget over 2 years, between 2015 and 2017, in the vicinity of the landslide. This means that the
river mainly acts as a sediment transfer zone and that river incision and sediment evacuation occurring along the river is
balanced by the sediment delivery occurring by the supply of landslide materials. This sediment supply may originate from
the several large landslides triggered in the Paolai area by the 2009 Morakot typhoon (Lin et al., 2011) and the following
massive sediment aggradation along fluvial valleys up to 10, 30 and even possibly 100 m (DeLisle and Yanites, 2018; Hsieh
and Capart, 2013). Our results would thus suggest that the Laonong river has not yet recovered from this aggradation phase
and that the landscape is still perturbed by the aftermath of Morakot typhoon, even 8 years after its occurrence. This exceeds
the relaxation time of 6 years observed after the 1999 Chi-Chi earthquake using river suspended load (Hovius et al., 2011).
But typhoon-triggered landslides occur every year in Taiwan, and global warming may intensify this process (Chiang and
Chang, 2011). This could also build and maintain long-term sediment sources within the Taiwan range, which will keep
supplying sediment into rivers even long after the Morakot-induced sources have been completely flushed.

6.2 Perspectives from recent progresses in gravimetry

In this study we take advantage of the intense surface processes occurring in Taiwan to jointly analyse both time-variable
gravity and photogrammetry measurements. Indeed, the amplitude of the sediment mass redistribution guarantees to measure
significant gravity changes and, most importantly, surface elevation changes. Nevertheless, for rivers experiencing large and
dynamic sediment mass redistributions that yet remain hidden beneath the water level, photogrammetric data would not bring
any constraint on the density inversion. One should thus only rely on the gravity measurements, leading to non-uniqueness
problem, since both the density and the location of the redistributed sediment would have to be inverted. To better deal with
this issue, we suggest two improvements to our gravity survey:

1. Set a denser network of gravity sites, ideally with a mesh structure. Indeed, more measurements, evenly distributed,
   mean more constraints on the density inversion.

2. Set this network closer to the mass changes to increase the gravity signal. The best option would be to locate the gravimeters directly beneath the river bottom. Fig. 11 shows that for such gravimeters, the average gravity change would increase from 31 to 50 µGal between 2016 and 2015 and from 13 to 61 µGal between 2017 and 2016.

This survey implies that gravimeters are set permanently over the time period of the project, as they won't be easily accessible. Such a setup of buried permanent gravimeters is presently impossible to realize with CG5 or any other contemporary relative or absolute gravimeter, but remains realistic at a few-years' timescale. Indeed, a new generation of relative gravimeters is rising from the use micro-electro-mechanical systems (MEMS) technology, characterized by a significantly smaller size and lower price (Liu and Pike, 2016; Middlemiss et al., 2016, 2017). Those shoebox-sized devices could be used to set permanent and dense gravity networks in rivers. However, setting persistent gravity networks in areas experiencing vigorous sediment transport shall require deeper practical thinking. Gravity changes densely sampled over the river will permit to retrieve the sediment mass redistribution using gravity inversion methods (e.g. Camacho et al., 2011) further constrained by the geometry of the river and the depth of the relative gravimeter. In addition, as relative gravimeters suffer from instrumental drift, this buried permanent network should be run in parallel to either permanent absolute measurements, which has recently become possible thanks to quantum gravimeters achieving 1 µGal repeatability (Ménoret et al., 2018), or to slowly drifting superconducting gravimeters (Hinderer et al., 2015). Therefore, ongoing progresses in the development of terrestrial gravimeters may open new opportunities for quantifying the mass of sediment redistributed by surface processes. Another interest for having such a permanent gravity network is to monitor the dynamics of the sediment mass redistribution at timescales shorter than one year, since the sediment concentration in Laonong river varies across the year (Fig. 12a).

6.3 Continuous sediment transport estimation

The method and perspectives introduced so far aim at quantifying the mass of sediment redistributed by an event with large sediment transport ability, such as a landslide or a high river discharge. The time step of this quantification depends on how long these events take to redistribute the sediment in a way that significantly alter the gravity measured at each site by, e.g., >10 µGal, as an indicative change. Nevertheless, the best solution is to set a permanent gravity network, so that any rapid sediment mass redistribution can be recorded. Fig. 12a shows that the largest sediment concentration recorded at LiuGui station is 5000 ppm (mass fraction), when the river level increased by 1.6 m.

For the hypothetical permanent buried gravity network (Fig. 11c), we compute the gravity effect of a river level change of 1.6 m, which covers the entire area of the active bed channel of Laonong River. The 5000-ppm sediment concentration means there is 5 kg of sediment in 1000 kg of river's fluid, hence 995 kg of pure water. In this framework, and assuming that the density of the sediment is 2×10^3 kg m^{-3}, we can compute the density change due to rising sediment concentrations, until 10^6 ppm, meaning the river is made of sediment only. The gravity variation solely due to a shift from 0 to 5000 ppm of suspended sediment is about 0.17 µGal on average over each site. This cannot be properly distinguished from the main gravity change

445   due to the rising river water level. In fact, the suspended sediment concentration would need to increase by about 3×10^5 ppm

to change the gravity by at least 10 µGal (Fig. 12b with the bedload set to 0 cm). This corresponds to a concentrated debris-

flow, nearly 8 times more concentrated than the threshold of 4×10^4 ppm used for debris-flow definition (Dadson et al., 2005;

Lin and Chen, 2013). However, sediment is also transported on the river bed, as bedload, and its variation must be added to

the variation of suspended sediment concentration to estimate the effect of sediment discharge variations on gravity. We have

450   no measurement of this bedload component for Laonong River but measurements in another catchment of Taiwan showed that

50% of the cumulative mass of the bedload was built by rocks which diameter is 15 cm (D_{50} = 150 mm) and D_{90} = 62.5 cm

(Cook et al., 2013). Therefore, we compute the effect of adding homogenous bedload layers of up to 60 cm thickness and

density 2×10^3 kg m^{-3} to suspended sediment variations (labelled curves in Fig. 12b). It generates about 50 µGal of gravity

variation, which would be clearly identifiable in the gravity measurements. This computation gives an order of magnitude of

455   the gravity change expected from time-varying suspended and bedload transport. It shows that continuous time-variable gravity

could quantify changes of sediment discharge if the sediment concentration rises by at least 3×10^5 ppm without bedload, or if

the bedload increases to a thickness of at least 12.5 cm, under the assumption that only gravity changes above 10 µGal are

significant. More accurate predictions of gravity effects require to know the proportionality relation, if any, between the

suspended and bedload component, as well as local hydrogravity models. Again, this 10-µGal threshold is linked to the

460   accuracy of todays' gravimeter but ongoing progresses and interest in time-variable gravimetry may fuel the development of

devices with higher accuracies.

7 Conclusion

This study shows that the mass of sediment redistributed by rivers and landslides can be estimated by combining time-lapse

gravimetric and photogrammetric measurements. Focusing on the Laonong River, in southern Taiwan, we estimate that

465   about $3.7 \pm 0.4\times10^9$ kg of sediment were removed from 2015 to 2017 around our study site. This sediment loss is mainly due

to a slow landslide moving from one year to another. The sediment budget (i.e. the difference between sedimentation and

erosion) within the river is close to zero, although more surveys should be carried out to identify longer-term deposition or

erosion in this area. The average sediment density obtained with this method ($1.9 \pm 0.01\times10^3$ kg m^{-3}) is similar to the average

sediment density measured in situ across the flood plain (2.0×10^3 kg m^{-3}). The new method introduced in this paper has the

470   advantage to directly sense the mass of sediment and can benefit a wealth of studies on surface processes, which require

quantitative estimates of sediment mass redistribution. Although time-variable gravimetry remains a rather expensive method

with demanding survey constraints, it has undergone promising progresses in the recent years. One is the significant

miniaturization of the devices, using inexpensive MEMS technology (Middlemiss et al., 2016), the other is the realization of

permanent absolute gravimeters, using cold-atom interferometry (Ménoret et al., 2018). Such new tools could be further used

475   without photogrammetry, for rivers where most of the sediment transport is hidden under the water. If the suspended and

bedload transport are significant enough, measuring the instantaneous sediment discharge could also become a reasonable project.

Data availability

All data are available in a public archive downloadable at this address:

480   https://chalmersuniversity.box.com/s/q5h1lpbflqlx9wi9yruway3k9jorflwe

Author contribution

P.S., M.M. and L.L conceived the study. M.M., N.L.M. and W.-C.H. acquired and processed the gravimetry data. K.-J.C. acquired and processed the photogrammetry data. L.J. and M.M. made the in situ sediment density measurements. C.H. acquired and processed the GPS-RTK data. J.-P.B. computed the hydrological loading effect on gravity. F.M initiated the

485   AGTO project. M.M. performed the main analysis. All authors contributed to the final form of the article.

Competing interests:

The authors declare that they have no conflict of interest.

Acknowledgments

M.M. did the fieldwork and part of the analysis study while ~~being~~ a postdoctoral researcher at Geosciences Rennes, supported

490   by a postdoctoral grant of the Centre National d'Etudes Spatiales (CNES) and by the CRITEX project funded by the Agence Nationale de la Recherche (ANR-11-EQPX-0011 and the Brittany region). We acknowledge support by the EROQUAKE project funded by the Agence Nationale de la Recherche (ANR-14-CE33-0005) and from the France-Taiwan International Associate Laboratory "From Deep Earth to Extreme Events" (LIA-D3E, http://www.lia-adept.org/). We are grateful to the RESIF-GMOB (http://www.resif.fr) facility for providing us with the relative gravimeter Scintrex CG5 #167. The authors

495   acknowledge the Taiwan Typhoon and Flood Research Institute, National Applied Research Laboratories, for providing the Data Bank for Atmospheric & Hydrologic Research service. Figs 1, 7 and 9 were done with GMT (Wessel et al., 2013). We thank three anonymous reviewers and associate editor Giulia Sofia, which comments improved the manuscript.

References

Aksoy, H. and Kavvas, M. L.: A review of hillslope and watershed scale erosion and sediment transport models, in Catena,

500   vol. 64, pp. 247–271., 2005.

Boedecker, G.: IAGBN: Absolute Observations Data Processing Standards, BGI-Bull. d'Information, 69, 25, 1991.

Bos, M. S. and Scherneck, H.-G.: Ocean tide loading provider, [online] Available from: http://holt.oso.chalmers.se/loading/, 2003.

Boy, J.-P.: EOST Loading Service, [online] Available from: http://loading.u-strasbg.fr/, 2015.

505   Camacho, A. G., Fernández, J. and Gottsmann, J.: The 3-D gravity inversion package GROWTH2.0 and its application to Tenerife Island, Spain, Comput. Geosci., 37(4), 621–633, doi:10.1016/j.cageo.2010.12.003, 2011.

Van Camp, M. and Vauterin, P.: Tsoft: graphical and interactive software for the analysis of time series and Earth tides, Comput. Geosci., 31(5), 631–640, doi:10.1016/j.cageo.2004.11.015, 2005.

Van Camp, M., Williams, S. D. P. and Francis, O.: Uncertainty of absolute gravity measurements, J. Geophys. Res., 110(B5), 510   B05406, doi:10.1029/2004JB003497, 2005.

Van Camp, M., de Viron, O., Scherneck, H.-G. G., Hinzen, K.-G. G., Williams, S. D. P., Lecocq, T., Quinif, Y. and Camelbeeck, T.: Repeated absolute gravity measurements for monitoring slow intraplate vertical deformation in western Europe, J. Geophys. Res., 116(B8), B08402, doi:10.1029/2010JB008174, 2011.

Van Camp, M., de Viron, O., Watlet, A., Meurers, B., Francis, O. and Caudron, C.: Geophysics From Terrestrial Time-Variable 515   Gravity Measurements, Rev. Geophys., 55(4), 938–992, doi:10.1002/2017RG000566, 2017.

Carbone, D. and Greco, F.: Review of Microgravity Observations at Mt. Etna: A Powerful Tool to Monitor and Study Active Volcanoes, Pure Appl. Geophys., 164(4), 769–790, doi:10.1007/s00024-007-0194-7, 2007.

Chang, K.-J., Chan, Y.-C., Chen, R.-F. and Hsieh, Y.-C.: Geomorphological evolution of landslides near an active normal fault in northern Taiwan, as revealed by lidar and unmanned aircraft system data, Nat. Hazards Earth Syst. Sci., 18(3), 709– 520   727, doi:10.5194/nhess-18-709-2018, 2018.

Chen, C. S. and Chen, Y. L.: The rainfall characteristics of Taiwan, Mon. Weather Rev., 131(7), 1323–1341, 2003.

Chiang, S. H. and Chang, K. T.: The potential impact of climate change on typhoon-triggered landslides in Taiwan, 2010-2099, Geomorphology, 133(3–4), 143–151, doi:10.1016/j.geomorph.2010.12.028, 2011.

Ching, K.-E. E., Hsieh, M.-L. L., Johnson, K. M., Chen, K.-H. H., Rau, R.-J. J. and Yang, M.: Modern vertical deformation 525   rates and mountain building in Taiwan from precise leveling and continuous GPS observations, 2000-2008, J. Geophys. Res., 116(B8), B08406, doi:10.1029/2011JB008242, 2011.

Cook, K. L., Turowski, J. M. and Hovius, N.: A demonstration of the importance of bedload transport for fluvial bedrock erosion and knickpoint propagation, Earth Surf. Process. Landforms, 38(7), 683–695, doi:10.1002/esp.3313, 2013.

Croissant, T., Lague, D., Steer, P. and Davy, P.: Rapid post-seismic landslide evacuation boosted by dynamic river width, Nat. 530   Geosci., 10, 680 [online] Available from: https://doi.org/10.1038/ngeo3005, 2017.

Crossley, D., Hinderer, J. and Riccardi, U.: The measurement of surface gravity., Rep. Prog. Phys., 76(4), 46101, doi:10.1088/0034-4885/76/4/046101, 2013.

Dadson, S., Hovius, N., Pegg, S., Dade, W. B., Horng, M. J. and Chen, H.: Hyperpycnal river flows from an active mountain belt, J. Geophys. Res. Earth Surf., 110(F4), n/a-n/a, doi:10.1029/2004JF000244, 2005.

535 Dadson, S. J., Hovius, N., Chen, H., Dade, W. B., Hsieh, M. L., Willett, S. D., Hu, J. C., Horng, M.-J. J., Chen, M.-C. C., Stark, C. P., Lague, D., Lin, J.-C. and others: Links between erosion, runoff variability and seismicity in the Taiwan orogen, Nature, 426(6967), 648–651 [online] Available from: http://dx.doi.org/10.1038/nature02150, 2003.

Darby, S. E., Hackney, C. R., Leyland, J., Kummu, M., Lauri, H., Parsons, D. R., Best, J. L., Nicholas, A. P. and Aalto, R.: Fluvial sediment supply to a mega-delta reduced by shifting tropical-cyclone activity, Nature, 539(7628), 276–279,
540 doi:10.1038/nature19809, 2016.

Deffontaines, B., Chang, K.-J., Champenois, J., Fruneau, B., Pathier, E., Hu, J.-C., Lu, S.-T. and Liu, Y.-C.: Active interseismic shallow deformation of the Pingting terraces (Longitudinal Valley – Eastern Taiwan) from UAV high-resolution topographic data combined with InSAR time series, Geomatics, Nat. Hazards Risk, 8(1), 120–136, doi:10.1080/19475705.2016.1181678, 2017.

545 Deffontaines, B., Chang, K.-J., Champenois, J., Lin, K.-C., Lee, C.-T., Chen, R.-F., Hu, J.-C. and Magalhaes, S.: Active tectonics of the onshore Hengchun Fault using UAS DSM combined with ALOS PS-InSAR time series (Southern Taiwan), Nat. Hazards Earth Syst. Sci., 18(3), 829–845, doi:10.5194/nhess-18-829-2018, 2018.

Dehant, V., Defraigne, P. and Wahr, J. M.: Tides for a convective Earth, J. Geophys. Res., 104, 1035–1058, 1999.

DeLisle, C. and Yanites, B. J.: The impacts of landslides triggered by the 2009 Typhoon Morakot on landscape evolution: A
550 mass balance approach, Am. Geophys. Union, Fall Meet. 2018, Abstr. #EP21C-2257 [online] Available from: http://adsabs.harvard.edu/abs/2018AGUFMEP21C2257D, 2018.

Eltner, A., Kaiser, A., Castillo, C., Rock, G., Neugirg, F. and Abellán, A.: Image-based surface reconstruction in geomorphometry – merits, limits and developments, Earth Surf. Dynam., 4(2), 359–389, doi:10.5194/esurf-4-359-2016, 2016.

Farinotti, D., Longuevergne, L., Moholdt, G., Duethmann, D., Mölg, T., Bolch, T., Vorogushyn, S. and Güntner, A.:
555 Substantial glacier mass loss in the Tien Shan over the past 50 years, Nat. Geosci., 8(9), 716–722, doi:10.1038/ngeo2513, 2015.

Ferguson, J. F., Klopping, F. J., Chen, T., Seibert, J. E., Hare, J. L. and Brady, J. L.: The 4D microgravity method for waterflood surveillance: Part 3 — 4D absolute microgravity surveys at Prudhoe Bay, Alaska, GEOPHYSICS, 73(6), WA163–WA171, doi:10.1190/1.2992510, 2008.

560 Ferro, V. and Porto, P.: Sediment Delivery Distributed (SEDD) Model, J. Hydrol. Eng., 5(4), 411–422, doi:10.1061/(ASCE)1084-0699(2000)5:4(411), 2000.

Fores, B., Champollion, C., Moigne, N. Le and Chery, J.: Impact of ambient temperature on spring-based relative gravimeter measurements, J. Geod., 91(3), 269–277, doi:10.1007/s00190-016-0961-2, 2017.

Furukawa, Y. and Ponce, J.: Accurate, dense, and robust multiview stereopsis, IEEE Trans. Pattern Anal. Mach. Intell., 32(8),
565 1362–1376, doi:10.1109/TPAMI.2009.161, 2010.

Ge, X., Li, T., Zhang, S. and Peng, M.: What causes the extremely heavy rainfall in Taiwan during Typhoon Morakot (2009)?, Atmos. Sci. Lett., 11(1), 46–50, 2010.

Gelaro, R., McCarty, W., Suárez, M. J., Todling, R., Molod, A., Takacs, L., Randles, C. A., Darmenov, A., Bosilovich, M. G.,

Reichle, R., Wargan, K., Coy, L., Cullather, R., Draper, C., Akella, S., Buchard, V., Conaty, A., da Silva, A. M., Gu, W., Kim, G.-K., Koster, R., Lucchesi, R., Merkova, D., Nielsen, J. E., Partyka, G., Pawson, S., Putman, W., Rienecker, M., Schubert, S. D., Sienkiewicz, M. and Zhao, B.: The Modern-Era Retrospective Analysis for Research and Applications, Version 2 (MERRA-2), J. Clim., 30(14), 5419–5454, doi:10.1175/JCLI-D-16-0758.1, 2017.

Han, S. C., Shum, C. K., Bevis, M., Ji, C. and Kuo, C.-Y.: Crustal Dilatation Observed by GRACE After the 2004 Sumatra-Andaman Earthquake, Science, 313(5787), 658–663, doi:10.1126/science.1128661, 2006.

Hare, J. L., Ferguson, J. F. and Brady, J. L.: The 4D microgravity method for waterflood surveillance: Part IV — Modeling and interpretation of early epoch 4D gravity surveys at Prudhoe Bay, Alaska, GEOPHYSICS, 73(6), WA173–WA180, doi:10.1190/1.2991120, 2008.

Hinderer, J., Crossley, D. and Warburton, R. J.: Superconducting Gravimetry, edited by G. B. T.-T. on G. (Second E. Schubert, pp. 59–115, Elsevier, Oxford., 2015.

Ho, C. S.: A synthesis of the geologic evolution of Taiwan, Tectonophysics, 125(1–3), 1–16, 1986.

Horton, A. J., Constantine, J. A., Hales, T. C., Goossens, B., Bruford, M. W. and Lazarus, E. D.: Modification of river meandering by tropical deforestation, Geology, 45(6), 511–514, doi:10.1130/G38740.1, 2017.

Hovius, N., Stark, C. P., Tsu, C. H., Chuan, L. J., Hao-tsu, C., Jiun-chuan, L., Chu, H. T. and Lin, J. C.: Supply and removal of sediment in a landslide-dominated mountain belt: Central Range, Taiwan, J. Geol., 108(1), 73–89, 2000.

Hovius, N., Meunier, P., Lin, C.-W. W., Chen, H., Chen, Y.-G. G., Dadson, S., Horng, M.-J. J. and Lines, M.: Prolonged seismically induced erosion and the mass balance of a large earthquake, Earth Planet. Sci. Lett., 304(3), 347–355, doi:10.1016/j.epsl.2011.02.005, 2011.

Hsieh, M.-L. and Capart, H.: Late Holocene episodic river aggradation along the Lao-nong River (southwestern Taiwan): An application to the Tseng-wen Reservoir Transbasin Diversion Project, Eng. Geol., 159, 83–97, doi:10.1016/J.ENGGEO.2013.03.019, 2013.

Hwang, C., Wang, C. G. and Lee, L. H.: Adjustment of relative gravity measurements using weighted and datum-free constraints, Comput. Geosci., 28(9), 1005–1015, 2002.

IES-AS: GPS LAB, [online] Available from: http://gps.earth.sinica.edu.tw/, 2015.

Jaboyedoff, M., Oppikofer, T., Abellán, A., Derron, M. H., Loye, A., Metzger, R. and Pedrazzini, A.: Use of LIDAR in landslide investigations: A review, Nat. Hazards, 61(1), 5–28, doi:10.1007/s11069-010-9634-2, 2012.

Jacob, T., Chery, J., Bayer, R., Le Moigne, N., Boy, J.-P., Vernant, P. and Boudin, F.: Time-lapse surface to depth gravity measurements on a karst system reveal the dominant role of the epikarst as a water storage entity, Geophys. J. Int., 177(2), 347–360, doi:10.1111/j.1365-246X.2009.04118.x, 2009.

Jacob, T., Bayer, R., Chery, J. and Le Moigne, N.: Time-lapse microgravity surveys reveal water storage heterogeneity of a karst aquifer, J. Geophys. Res., 115(B6), B06402, doi:10.1029/2009JB006616, 2010.

Kao, R., Hwang, C., Kim, J. W., Ching, K.-E., Masson, F., Hsieh, W.-C., Le Moigne, N. and Cheng, C.-C.: Absolute gravity change in Taiwan: Present result of geodynamic process investigation., Terr. Atmos. Ocean. Sci., 28(6), 855–875 [online]

Available from: http://10.0.12.247/TAO.2017.06.13.01, 2017.

Kazama, T., Okubo, S., Sugano, T., Matsumoto, S., Sun, W., Tanaka, Y. and Koyama, E.: Absolute gravity change associated with magma mass movement in the conduit of Asama Volcano (Central Japan), revealed by physical modeling of hydrological gravity disturbances, J. Geophys. Res., 1263–1287, doi:10.1002/2014JB011563, 2015.

Letellier, T., Lyard, F. and Lefèvre, F.: The new global tidal solution: FES2004, in Proceedings of the Ocean Surface Topography Science Team Meeting, St. Petersburg, Florida, pp. 4–6., 2004.

Lin, C.-W., Chang, W.-S., Liu, S.-H., Tsai, T.-T., Lee, S.-P., Tsang, Y.-C., Shieh, C.-L. and Tseng, C.-M.: Landslides triggered by the 7 August 2009 Typhoon Morakot in southern Taiwan, Eng. Geol., 123(1), 3–12, doi:https://doi.org/10.1016/j.enggeo.2011.06.007, 2011.

Lin, G.-W. and Chen, H.: Recurrence of hyper-concentration flows on the orogenic, subtropical island of Taiwan, J. Hydrol., 502, 139–144, doi:10.1016/J.JHYDROL.2013.08.036, 2013.

Liu, H. and Pike, W. T.: A micromachined angular-acceleration sensor for geophysical applications, Appl. Phys. Lett., 109(17), 173506, doi:10.1063/1.4966547, 2016.

Liu, Y.-C., Hwang, C., Han, J., Kao, R., Wu, C.-R., Shih, H.-C. and Tangdamrongsub, N.: Sediment-Mass Accumulation Rate and Variability in the East China Sea Detected by GRACE, Remote Sens., 8(10), 777, doi:10.3390/rs8090777, 2016.

Longuevergne, L., Boy, J.-P., Florsch, N., Viville, D., Ferhat, G., Ulrich, P., Luck, B. and Hinderer, J.: Local and global hydrological contributions to gravity variations observed in Strasbourg, J. Geodyn., 48(3–5), 189–194, doi:10.1016/j.jog.2009.09.008, 2009.

Longuevergne, L., Wilson, C. R., Scanlon, B. R. and Crétaux, J. F.: GRACE water storage estimates for the middle east and other regions with significant reservoir and lake storage, Hydrol. Earth Syst. Sci., 17(12), 4817–4830, doi:10.5194/hess-17-4817-2013, 2013.

Ménoret, V., Vermeulen, P., Le Moigne, N., Bonvalot, S., Bouyer, P., Landragin, A. and Desruelle, B.: Gravity measurements below 10-9g with a transportable absolute quantum gravimeter, Sci. Rep., 8(1), 1–11, doi:10.1038/s41598-018-30608-1, 2018.

Merriam, J. B.: Atmospheric pressure and gravity, Geophys. J. Int., 109(3), 488–500, doi:10.1111/j.1365-246X.1992.tb00112.x, 1992.

Middlemiss, R. P., Samarelli, A., Paul, D. J., Hough, J., Rowan, S. and Hammond, G. D.: The First Measurement of the Earth Tides with a MEMS Gravimeter, Nature, 531, 614–617, doi:10.1038/nature17397, 2016.

Middlemiss, R. P., Bramsiepe, S. G., Douglas, R., Hough, J., Paul, D. J., Rowan, S. and Hammond, G. D.: Field tests of a portable MEMS gravimeter, Sensors (Switzerland), 17(11), 1–12, doi:10.3390/s17112571, 2017.

Milliman, J. D. and Farnsworth, K. L.: River Discharge to the Coastal Ocean: A Global Synthesis., 2011.

Molnar, P., Anderson, R. S. and Anderson, S. P.: Tectonics, fracturing of rock, and erosion, J. Geophys. Res. Earth Surf., 112(3), 1–12, doi:10.1029/2005JF000433, 2007.

Morera, S. B., Condom, T., Crave, A., Steer, P. and Guyot, J. L.: The impact of extreme El Niño events on modern sediment transport along the western Peruvian Andes (1968–2012), Sci. Rep., 7(1), 11947, doi:10.1038/s41598-017-12220-x, 2017.

Mouyen, M., Masson, F., Hwang, C., Cheng, C.-C. C., Moigne, N. Le, Lee, C. .-. W., Kao, R., Hsieh, W.-C. C., Le Moigne, N., Lee, C. .-. W., Kao, R., Hsieh, W.-C. C., Moigne, N. Le, Lee, C. .-. W., Kao, R. and Hsieh, W.-C. C.: Erosion effects assessed by repeated gravity measurements in southern Taiwan, Geophys. J. Int., 192(1), 113–136, doi:10.1093/gji/ggs019, 2013.

Mouyen, M., Longuevergne, L., Steer, P., Crave, A., Lemoine, J.-M. J. M., Save, H. and Robin, C.: Assessing modern river sediment discharge to the ocean using satellite gravimetry, Nat. Commun., 9(1), 3384, doi:10.1038/s41467-018-05921-y, 2018.

Nagy, D.: The prism method for terrain corrections using digital computers, Pure Appl. Geophys., 63(1), 31–39, doi:10.1007/BF00875156, 1966.

Naujoks, M., Weise, a., Kroner, C. and Jahr, T.: Detection of small hydrological variations in gravity by repeated observations with relative gravimeters, , 82(9), 543–553, doi:10.1007/s00190-007-0202-9, n.d.

Niebauer, T. M.: Gravimetric methods – absolute gravimeter : instruments concepts and implementation, in Treatise on Geophysics, vol. 3, edited by G. Schubert, pp. 37–57, Elsevier., 2015.

Niebauer, T. M., Sasagawa, G. S., Faller, J. E., Hilt, R. and Klopping, F.: A new generation of absolute gravimeters, Metrologia, 32, 159–180, 1995.

Niethammer, U., James, M. R., Rothmund, S., Travelletti, J. and Joswig, M.: UAV-based remote sensing of the Super-Sauze landslide: Evaluation and results, Eng. Geol., 128, 2–11, doi:https://doi.org/10.1016/j.enggeo.2011.03.012, 2012.

Oborne, M.: Mission Planner, [online] Available from: https://ardupilot.org/planner/ (Accessed 10 April 2020), 2010.

Pail, R., Bingham, R., Braitenberg, C., Dobslaw, H., Eicker, A., Güntner, A., Horwath, M., Ivins, E., Longuevergne, L., Panet, I. and Wouters, B.: Science and User Needs for Observing Global Mass Transport to Understand Global Change and to Benefit Society, Surv. Geophys., 36(6), 743–772, doi:10.1007/s10712-015-9348-9, 2015.

Peizhen, Z., Molnar, P. and Downs, W. R.: Increased sedimentation rates and grain sizes 2-4 Myr ago due to the influence of climate change on erosion rates, Nature, 410(April), 891–897, doi:10.1038/35073504, 2001.

Petrov, L. and Boy, J.-P.: Study of the atmospheric pressure loading signal in very long baseline interferometry observations, J. Geophys. Res., 109(B3), B03405, doi:10.1029/2003JB002500, 2004.

Pfeffer, J., Champollion, C., Favreau, G., Cappelaere, B., Hinderer, J., Boucher, M., Nazoumou, Y., Oï, M., Mouyen, M., Henri, C., Moigne, N. Le, Deroussi, S., Demarty, J., Boulain, N., Benarrosh, N., Robert, O., Le Moigne, N., Deroussi, S., Demarty, J., Boulain, N., Benarrosh, N. and Robert, O.: Evaluating surface and subsurface water storage variations at small time and space scales from relative gravity measurements in semiarid Niger, Water Resour. Res., 49(6), doi:10.1002/wrcr.20235, 2013.

Pix4D: Pix4Dmapper: professional drone mapping and photogrammetry software, [online] Available from: https://www.pix4d.com/product/pix4dmapper-photogrammetry-software (Accessed 10 April 2020), 2020.

Rebischung, P., Griffiths, J., Ray, J., Schmid, R., Collilieux, X. and Garayt, B.: IGS08: The IGS realization of ITRF2008, GPS Solut., 16(4), 483–494, doi:10.1007/s10291-011-0248-2, 2012.

Rodell, M., Houser, P. R., Jambor, U., Gottschalck, J., Mitchell, K., Meng, C.-J. J., Arsenault, K., Cosgrove, B., Radakovich, J., Bosilovich, M., Entin*, J. K., Walker, J. P., Lohmann, D., Toll, D., Entin, J. K., Walker, J. P., Lohmann, D. and Toll, D.: The Global Land Data Assimilation System, B. Am. Meteorol. Soc., 85(3), 381–394, doi:10.1175/BAMS-85-3-381, 2004.

Schwab, M., Rieke-Zapp, D., Schneider, H., Liniger, M. and Schlunegger, F.: Landsliding and sediment flux in the Central
675 Swiss Alps: A photogrammetric study of the Schimbrig landslide, Entlebuch, Geomorphology, 97(3), 392–406, doi:https://doi.org/10.1016/j.geomorph.2007.08.019, 2008.

Scintrex Ltd.: CG-5 Scintrex Autograv System, Operation Manual, Scintrex Limited, Concord, Ontario, Canada, http://www.scintrexltd.com/., 2010.

Seitz, S. M., Curless, B., Diebel, J., Scharstein, D. and Szeliski, R.: A comparison and evaluation of multi-view stereo
680 reconstruction algorithms, in Proceedings of the IEEE Computer Society Conference on Computer Vision and Pattern Recognition, vol. 1, pp. 519–526., 2006.

Steer, P., Huismans, R. S., Valla, P. G., Gac, S. and Herman, F.: Bimodal plio-quaternary glacial erosion of fjords and low-relief surfaces in Scandinavia, Nat. Geosci., 5(9), 635–639, doi:10.1038/ngeo1549, 2012.

Steer, P., Simoes, M., Cattin, R. and Shyu, J. B. H.: Erosion influences the seismicity of active thrust faults., Nat. Commun.,
685 5, 5564, doi:10.1038/ncomms6564, 2014.

Taiwan Water Resources Agency: Hydrological Year Book of Taiwan Republic of China, 2019.

Tapley, B. D., Bettadpur, S., Ries, J. C., Thompson, P. F. and Watkins, M. M.: GRACE measurements of mass variability in the Earth system, Science, 305(5683), 503–505, doi:10.1126/science.1099192, 2004.

Torres, A., Brandt, J., Lear, K. and Liu, J.: A looming tragedy of the sand commons, Science, 357(6355), 970–971,
690 doi:10.1126/science.aao0503, 2017.

Tu, J. T., Chou, C. and Chu, P. S.: The abrupt shift of typhoon activity in the vicinity of Taiwan and its association with western North Pacific-East Asian climate change, J. Clim., 22(13), 3617–3628, doi:10.1175/2009JCLI2411.1, 2009.

Wessel, P., Smith, W. H. F., Scharroo, R., Luis, J. and Wobbe, F.: Generic Mapping Tools: Improved Version Released, Eos, Trans. Am. Geophys. Union, 94(45), 409–410, doi:10.1002/2013EO450001, 2013.

695 Willett, S. D.: Orogeny and orography: The effects of erosion on the structure of mountain belts, J. Geophys. Res., 104(B12), 928–957, doi:10.1029/1999JB900248, 1999.

700

Appendix A: Processing of the relative gravity survey

Figures A1, A2 and A3 summarize how each relative survey were done in 2015, 2016 and 2017, respectively. All relative
705 loops start and end at AG06 and other relative gravity sites (prefix BA) are re-measured several time for each survey, within
a few hours. It is necessary to have such repeated measures in order to estimate and remove the instrumental drift of the CG5
relative gravimeter. The adjustment is done using the software Gravnet (Hwang et al., 2002), assuming drift linear with time.
The instrumental drift for each year are:

2015: 0.032 ± 0.037 mGal day^{-1}

710 2016: -0.085 ± 0.004 mGal day^{-1}

2017: -0.161 ± 0.007 mGal day^{-1}

Appendix B: Gravimetric effect of the dolosse

Fig. B1a is a picture of the dolosse stacked near the gravity site BA02. Their side L and height H are reported with blue lines for comparison with Figs. B1c-d. They are made of 3 identical patterns, which repeats around the center of the dolosse, and close it. The center of the dolosse and part of his sides are empty. However, due to its limited spatial resolution, the photogrammetry "sees" the dolosse as plain hexagons (Fig. B1b). Our aim is thus to define the ratio k between an actual dolosse and a plain dolosse. This ratio is then multiplied by the average density ρ_c of concrete (2.3×10^3 kg m^{-3}), which the dolosse are made of. This way we obtain an effective dolosse density that we pair to the volume obtained from the photogrammetry and eventually compute the gravitational effect of the dolosse at our study sites.

The volume Vp of a regular hexagon with side L and height H is

$$V = \frac{3}{2}\sqrt{3}L^2H = 4.9 \text{ m}^3 \tag{A1}$$

The volume Vd of the actual dolosse is estimated to 1.6 m^3, using the geometry detailed in Figs. B1c-d.

Therefore, we find that the true volume of the dolosse is $k = 1.6/4.9 \cong 0.33$, that is one third of the plain volume, hence its effective density is $2.3k = 0.76\times10^3$ kg m^{-3}. The geometry and density of the dolosse were used to compute their gravitational attraction at BA04 and BA05 using gravity modelling by rectangular prisms methods (Nagy, 1966). This effect is about -15 µGal.

730 **Appendix C: In situ determination of the river materials density**

Site selection:
We select 20 sites in the active river channel, which are accessible by walking. We try to find sites where materials are different, some of them being close to each other, to better grasp the variety of the material in the channel. Nevertheless, we also try to
735 have a spatially even sampling. In a few places, two sampling are done at the same horizontal position but at the surface and then deeper. All sites positions are recorded with a hand gps (about 3 m accuracy).

Material sampling
At each start, we first distribute several benchmarked rules all around the place that will be sampled (Fig. C1a). Several pictures
740 are taken to cover the sampling site and several benchmarked rules at a time. Pictures should overlap each other. We then dig a hole of about 30- 40cm depth and radius, paying attention to not move any of the benchmarked rules. The excavated material M is put in a bucket of known mass and weighted using a hook-hanging weight machine. Then another set of pictures is taken to cover again the benchmarked rules and the hole just dug. The only difference between the pictures taken before and after is the hole.
745

Photogrammetry:
The benchmarked rules make a common reference between the pictures taken before and after the hole is dug. They are transformed into clouds of points in 3D (Fig. C1b), one representing the original surface, the other representing the dug surface. Thus, subtracting these two surfaces returns the surface of the hole, from which the volume V of the hole is computed (Fig.
750 C1c).

Density computation:
The density at the sampling site is then M divide by V.

755

Tables

760

Effect	Method	Order of magnitude [μGal]	Uncertainty [μGal]	Correction applied
Solid earth tides	WDD	100	0.1	Before the adjustment
Ocean tide loading	FES 2004 model	10	0.1	Before the adjustment
Polar motions	IERS data	1	0.1	Before the adjustment
Air pressure	Barometer data	0.5-1	0.1	Before the adjustment
Vertical ground motions	GNSS data	-2-4	1-2	After the adjustment
Hydrology	GLDAS2/MERRA2 model	2	5	After the adjustment
Dolosse at BA03, BA04	Photogrammetry	-15	5	After the adjustment

Table 1: Summary of the corrections applied to our gravity measurements, with their order of magnitude and a statement on whether there are applied before or after the drift adjustment. The uncertainties on the first four corrections are those proposed by Van Camp et al., 2005.

Survey	Images used (total number of images)	Number of GCP used	Average GSD (cm)	Mean re-projection error (in pixel)
2015	2148 (2389)	11	21.75	0.151
2016	2524 (2556)	13	15.63	0.132
2017	681 (683)	15	15.42	0.175

Table 2: Image processing summary

Point cloud densification	DSM parameters
Image scale: half of the image size	Resolution: 1GSD
Minimum number of matching: 4	Noise filter on
Point density: Optimal	Surface smoothing: sharp
DSM parameters	Inverse distance weighting

Table 3: Processing parameters set in Pix4D

Check Points	Δz 2015 (m)	Δz 2016 (m)	Δz 2017 (m)
CKP 1	0.04	0.65	-0.21
CKP 2	-0.03	0.43	-0.02
CKP 3	0.36	0.01	0.05
CKP 4	0.21	0.02	0.15
CKP 5	0.17	-0.11	0.09
CKP 6	0.26	-0.05	0.10
CKP 7	0.16	-0.54	0.19
CKP 8	0.24	-0.33	NA
CKP 9	-0.32	-0.20	-0.51
CKP 10	0.18	-0.01	-0.42
CKP 11	-1.95	-0.49	0.97
Standard deviation	**0.65**	**0.35**	**0.40**
Standard error	**0.20**	**0.11**	**0.13**

Table 4: Results of field check points and the elevation difference (Δz) of photogrammetric DSM for each survey

Site	2015	2016	2017
AG06	978713849.3 ± 1.6	978713845.2 ± 0.9	978713845.7 ± 3
BA01	-795.7 ± 1.3	-793.7 ± 1.8	-799.9 ± 1.8
BA02	-474.5 ± 2.1	-489.9 ± 2.0	No value
BA03	-204.9 ± 2.6	-176.7 ± 2.0	-217.2 ± 6.6
BA04	292.8 ± 2.4	347.3 ± 2.3	300.5 ± 6.8
BA05	673.8 ± 2.6	715.1 ± 2.3	718.8 ± 1.4
BA06	901.9 ± 2.4	960.6 ± 2.4	965.6 ± 1.4
BA07	1188.8 ± 2.4	1254.4 ± 2.4	1240.8 ± 1.5
BA08	1637.7 ± 2.1	1666.2 ± 2.2	1653.7 ± 1.8
BA09	1932.4 ± 1.4	1928.0 ± 2.8	1906.5 ± 1.3

Table 5: Gravity values measured at each site for all surveys, in μGal. The values at each relative gravity site (BA) are given relative to the absolute value measured at AG06.

Case	Densities (10^3 kg m^{-3})		RMS (μGal)
	River	**Landslide**	
1	$\rho = 1.9 \pm 0.01$ (no distinction river/landslide)		9.6
2	$\rho_r = 1.9 \pm 0.01$	$\rho_l = 2.0 \pm 0.1$	9.5
3	$\rho_r^{1615} = 1.6 \pm 0.1$; $\rho_r^{1716} = 2.0 \pm 0.01$	$\rho_l = 1.7 \pm 0.3$	9.6

Table 6: Densities obtained for each inversion case, with their standard deviation and the root mean square of the residuals _V_.
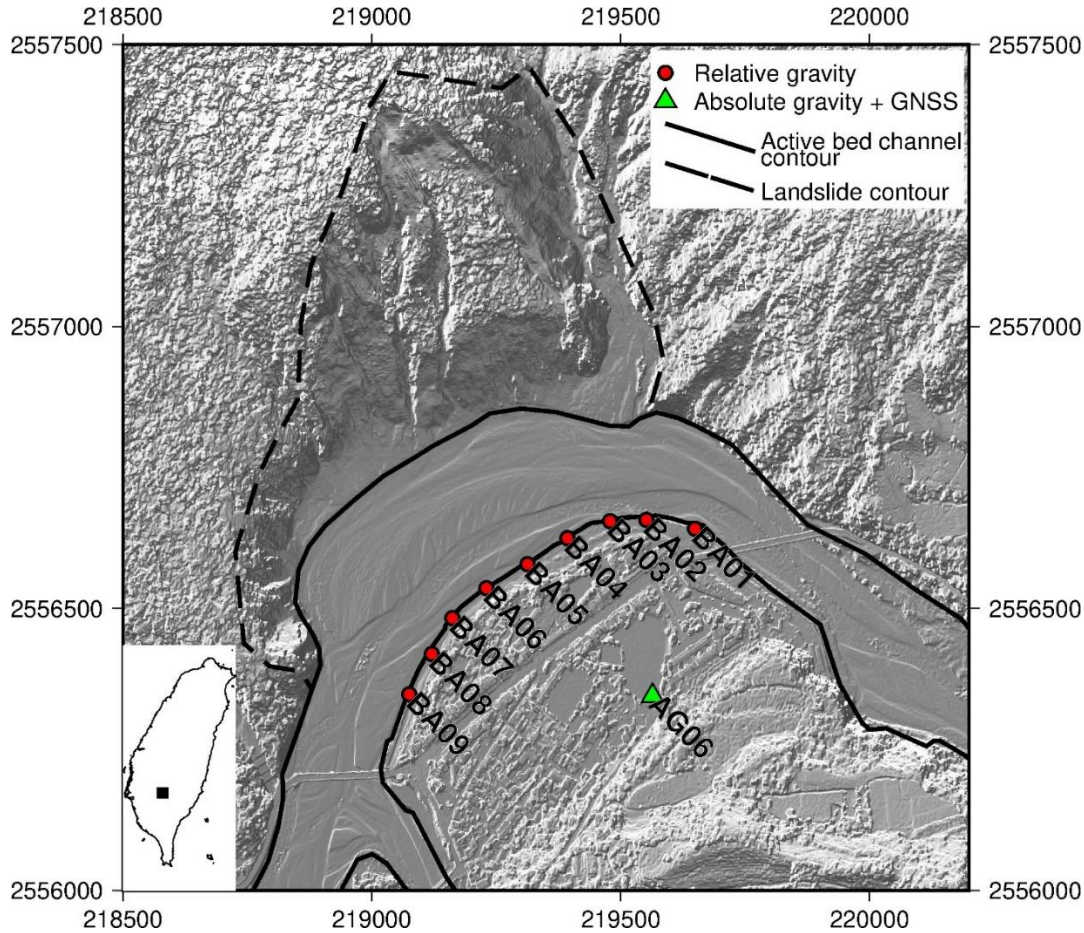
795
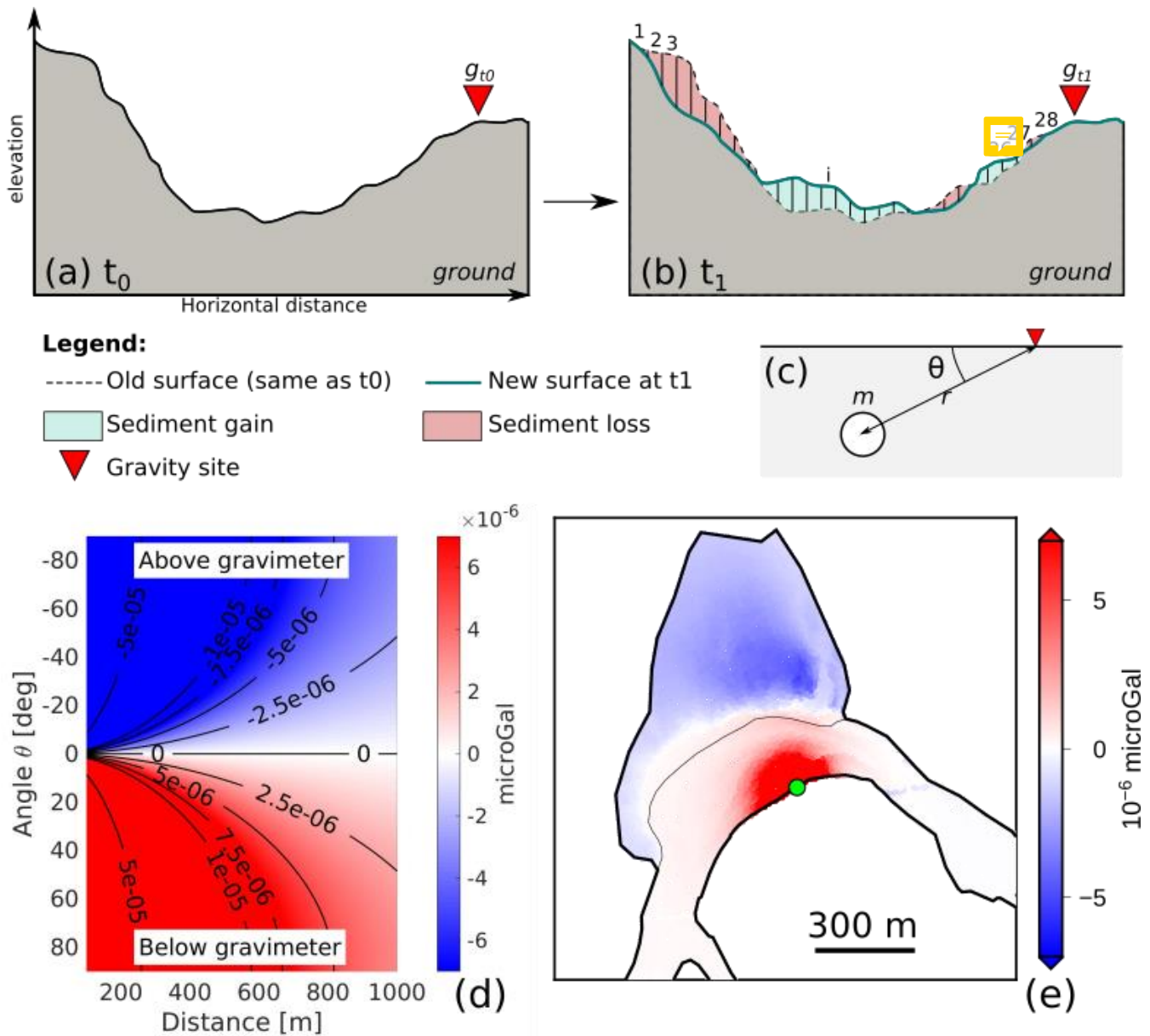
Figure 2: a) Ground surface elevation at time t_0, gravity is measured and equal to g_{t0}. **b)** New ground surface at $t_1 > t_0$, after sediment mass redistributions occurred. The gravity is measured again at the same place and is equal to g_{t1}. **c)** Parameters used for computing a point-mass gravity effect (equation 1, point-mass means that the element is approximated to a point which mass is that of the element). **d)** Theoretical effect of a 2000-kg point mass as a function to its distance and angle (Eq. 1) from the gravimeter. **e)** Synthetic gravity effect at one measurement site (green dot, actually BA04) for each mass element located at the surface of the Paolai river bed or landslide. A mass element is a 0.5x0.5x1 m rectangular prisms of density 2, which height is given by the actual topography of the area (Fig. 1). The actual gravity effect measured at the green site is the sum of each element gravity effect. The colorscale is saturated to highlight the change of sign across the landslide area.
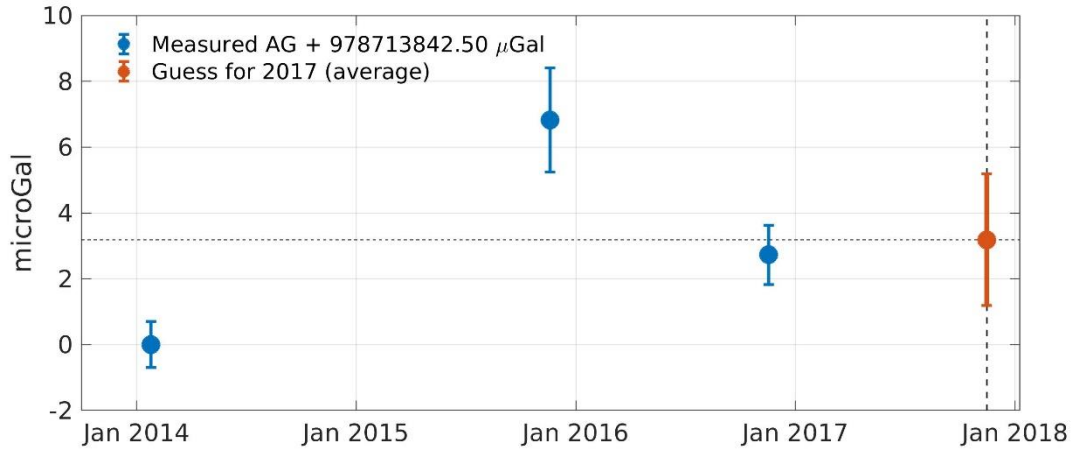
Figure 3: Absolute gravity values measured at AG06 in 2014 (January 25), 2015 (November 20) and 2016 (November 18). In 2017 (November 16), the absolute gravimeter suffered from a laser problem and no measurement could be done. We thus consider that the value in 2017 is the average of the 2014, 2015 and 2016 values. These absolute gravity values are already corrected for tides, air pressure and polar motions, but not for hydrology and vertical ground displacements yet. The error bar for the values in 2014, 2015 and 2016 combine the measurement uncertainty obtained during each a gravity survey and the uncertainties due to the tides, air pressure and polar motions corrections.
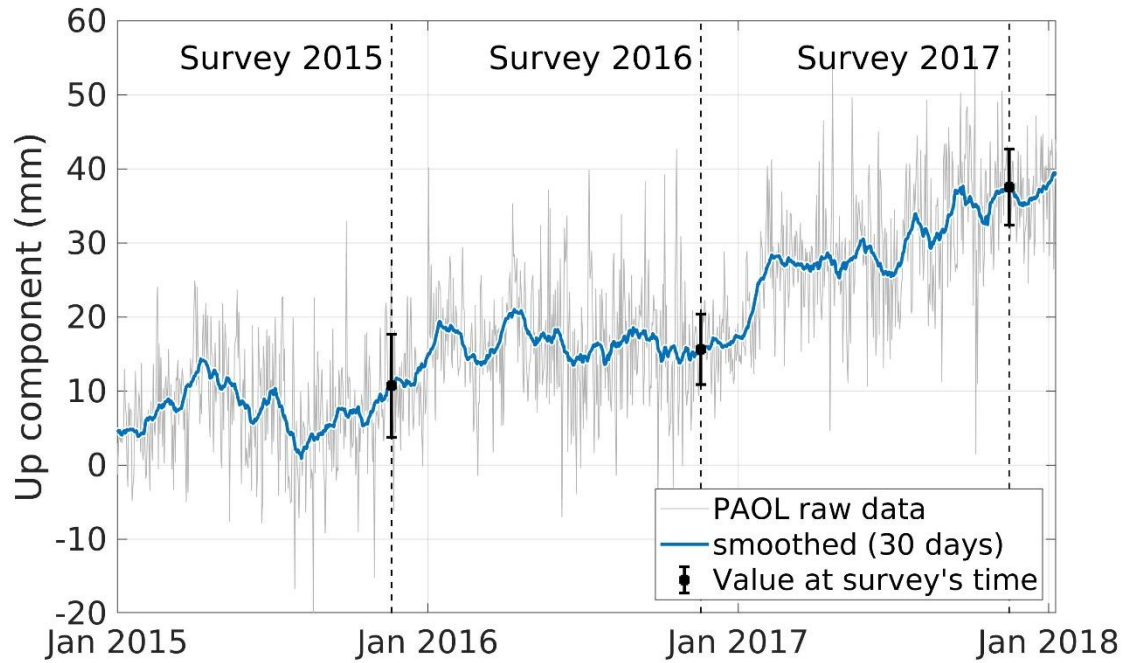
Figure 4: Ground vertical displacements time series at PAOL GNSS station, co-located with AG06, provided by the GPSLAB database (IES-AS, 2015)**. Solutions are computed in the IGS08 reference frame** (Rebischung et al., 2012)**. The time of each joined gravity and photogrammetry survey is shown by dotted lines. The error bar is computed from the standard deviation of the measurements of the same 30-days window.**

820

825
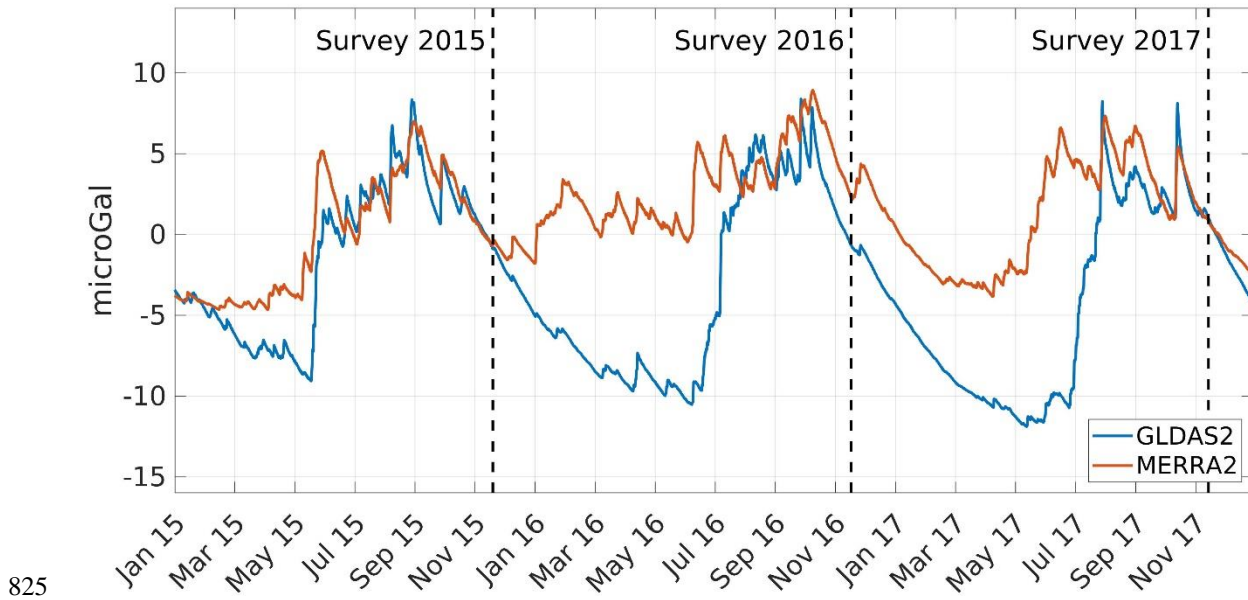
Figure 5: Hydrological effect on gravity at AG06, estimated from global hydrological models GLDAS2 and MERRA2.
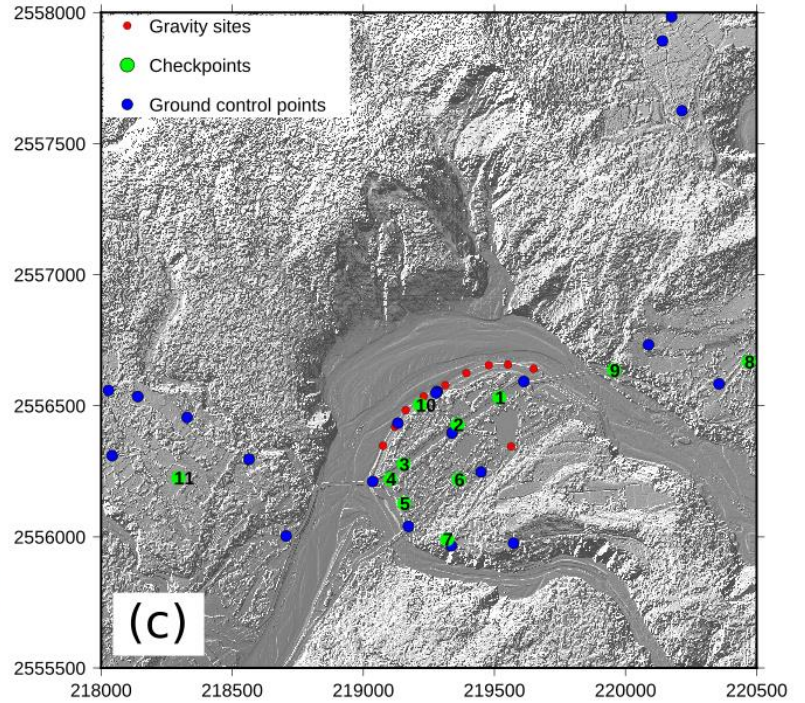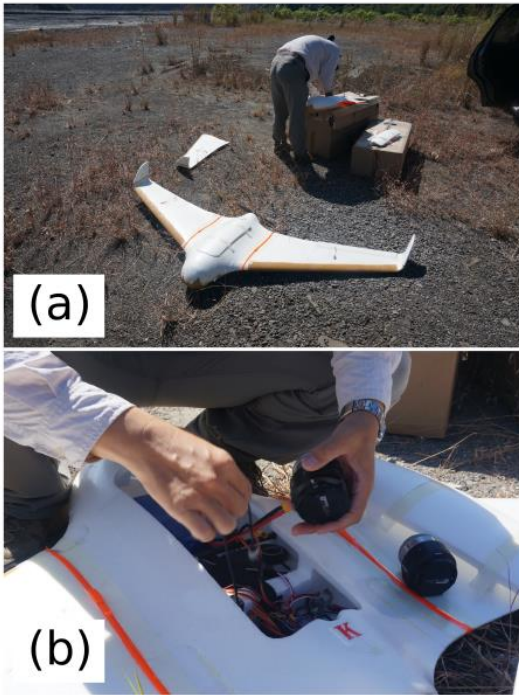
830

Figure 6: a) UAV, modified Skywalker X8. b) Close-up on the central compartment of the UAV, where the camera and lens are mounted. c) Map of the ground control points and checkpoints (numbered according to Table 4) with the shaded topography in the background. The gravity sites are also shown for reference.

835
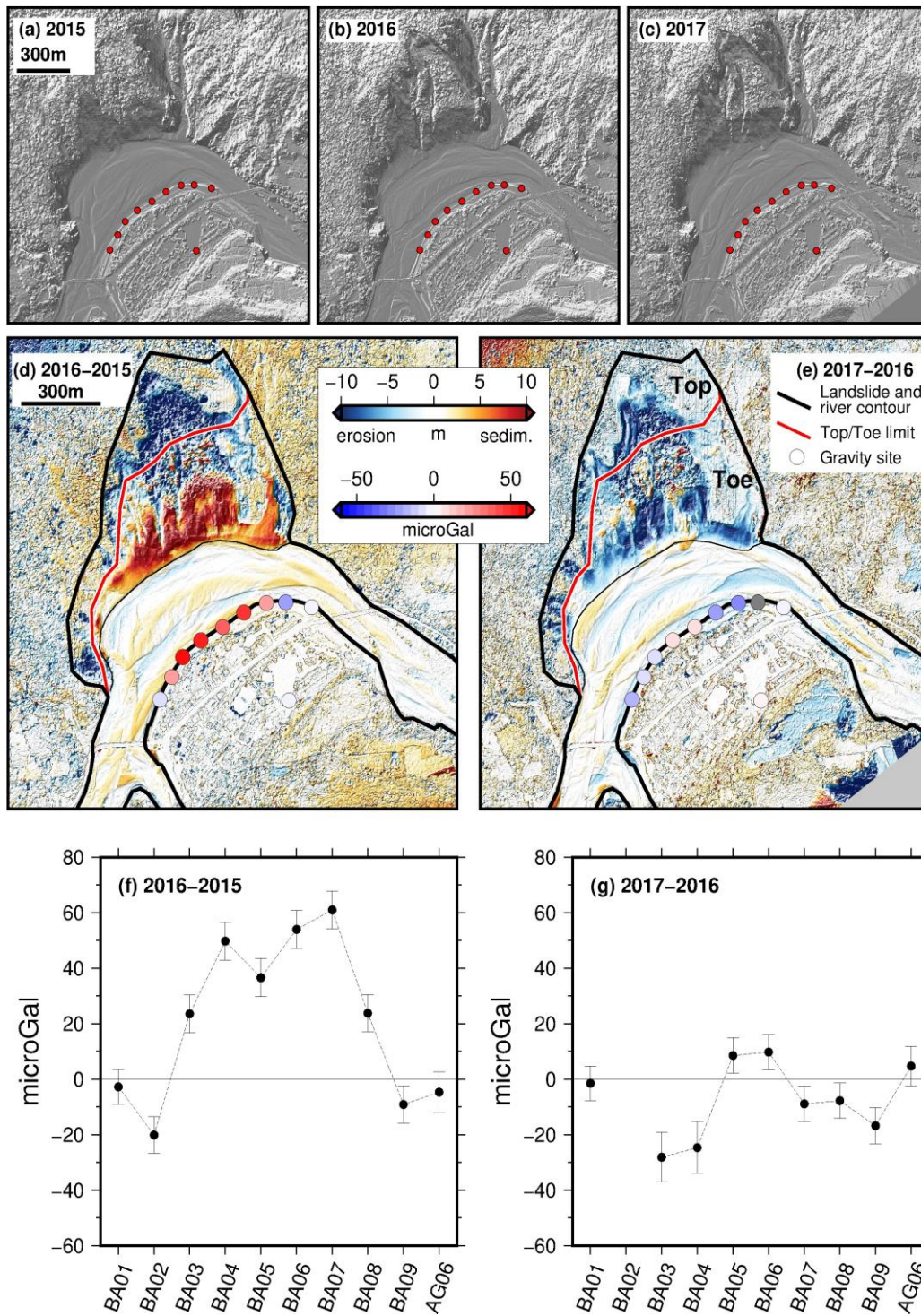
Figure 7: The digital surface models in a) 2015, b) 2016 and c) 2017 and their differences d) between 2016 and 2015 and e) between 2017 and 2016. The disks that locate the gravity sites are colored relative to the gravity change. The black contour line limits the

river and the landsliding area. The landsliding area is divided into two parts: the top and the toe. The color scale of the elevation changes is bounded within ±10 m, which contains 92% of the elevation changes between 2015 and 2016, and 96% of the elevation changes between 2016 and 2017. The extrema are -46 m/33 m between 2015 and 2016, and -38 m/33 m between 2016 and 2017. (f) Gravity changes between 2015 and 2016 . (g) Gravity changes between 2016 and 2017. BA02 could not be measured in 2017 because of construction work ongoing near the site. The error bars represent $\sqrt{\sum_i \sigma_i^2}$ where σ's are the uncertainties of the gravity measurements after the instrumental drift adjustment and of the seven corrections given in Table 1 (thus i ranges from 1 to 8).
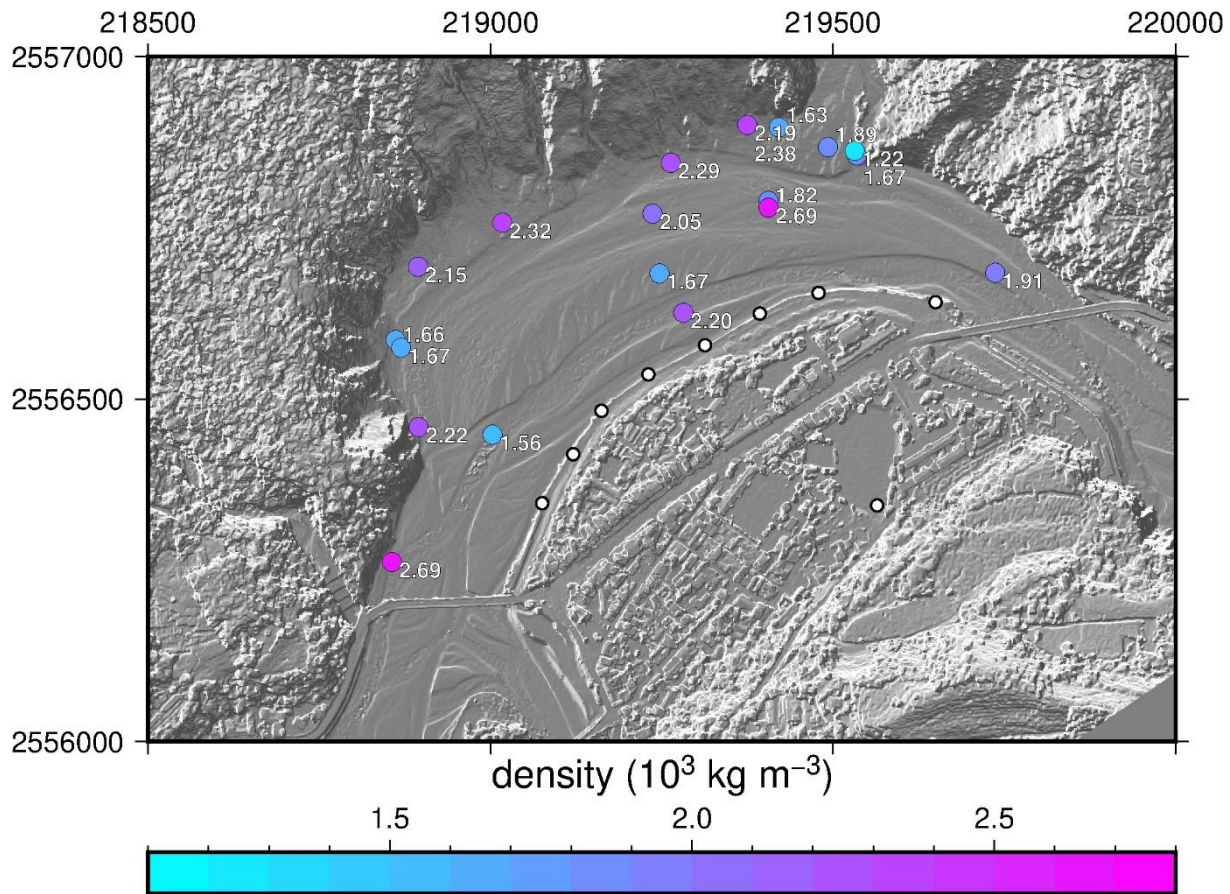
Figure 8: In situ density measured during the 2017 survey (colored dots, the value is also reported in white). Gravity sites are shown with white dots. Axes are in meters. The background is the shaded topography measured during the 2017 survey.
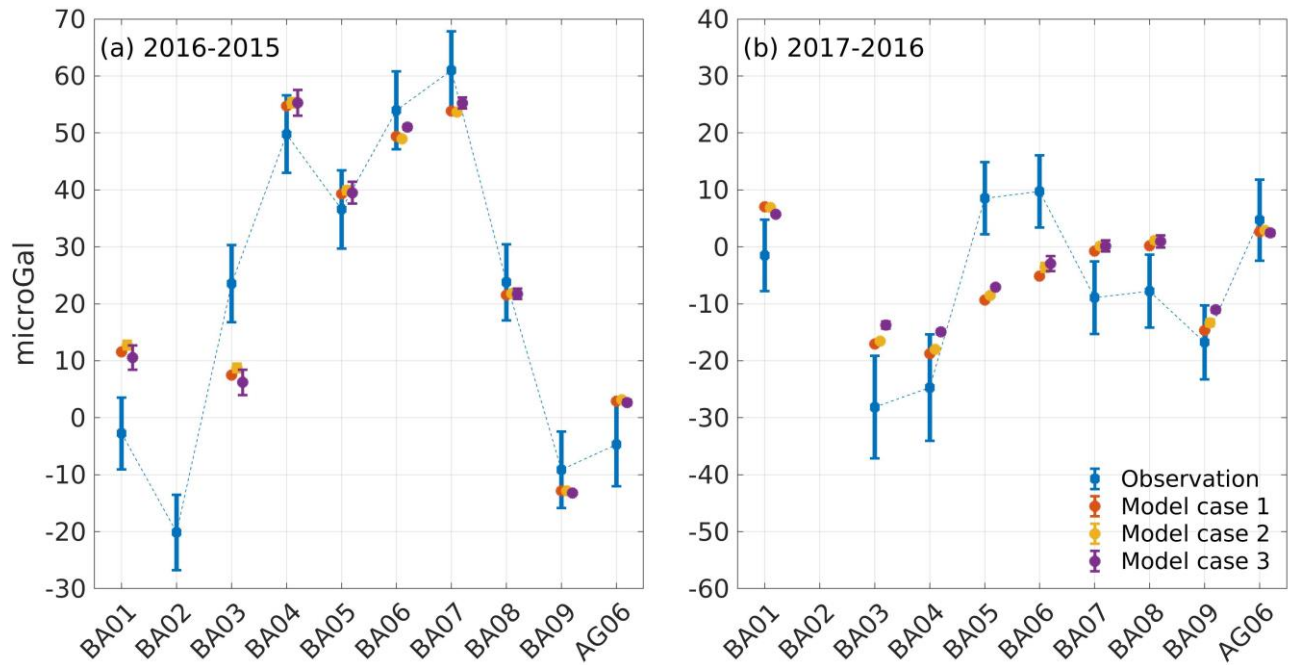
Figure 9: Comparison of the observed (blue) and modelled gravity changes for the densities inverted in cases 1, 2 and 3 (red, yellow and purple, respectively). Each case is slightly offset horizontally for legibility. No gravity is estimated at BA02 since its location is unknown.
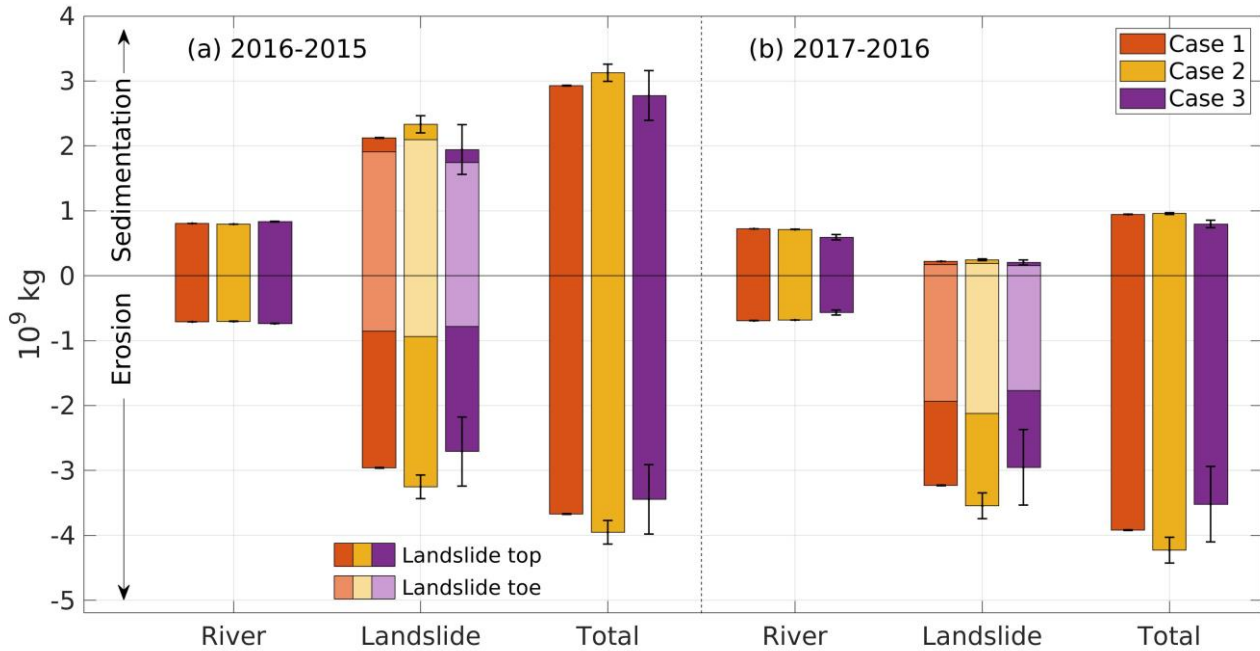
Figure 10: Estimation of the mass of sediment redistributed between 2016 and 2015, and between 2017 and 2016 in cases 1, 2 and 3 (red, yellow and purple, respectively; same color code as in Fig. 9). The mass estimation is shown for the river, the landslide and their sum (total). The error bars are computed by multiplying the volumes variations from the DSM with the densities uncertainties (Table 6). The landslide volumes distinguish the top and the toe of the landslides with a stacked bar plot form.
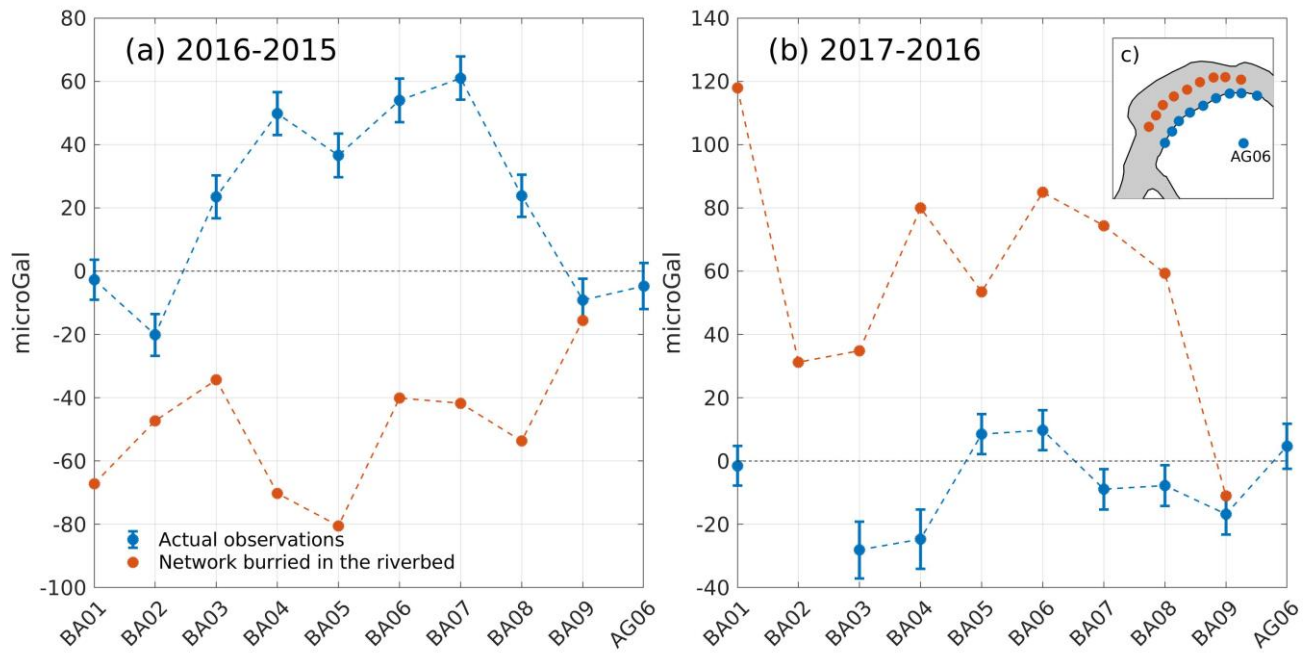
Figure 11: Gravity changes expected at new sites located 5 m beneath the river (red), compared with those measured at BA01-BA09 (blue), for the same sediment mass redistributions as a) between 2015 and 2016 and b) between 2016 and 2017. The new sites are in fact BA01 – BA09 translated 140 m in the north-east direction, as illustrated in c).
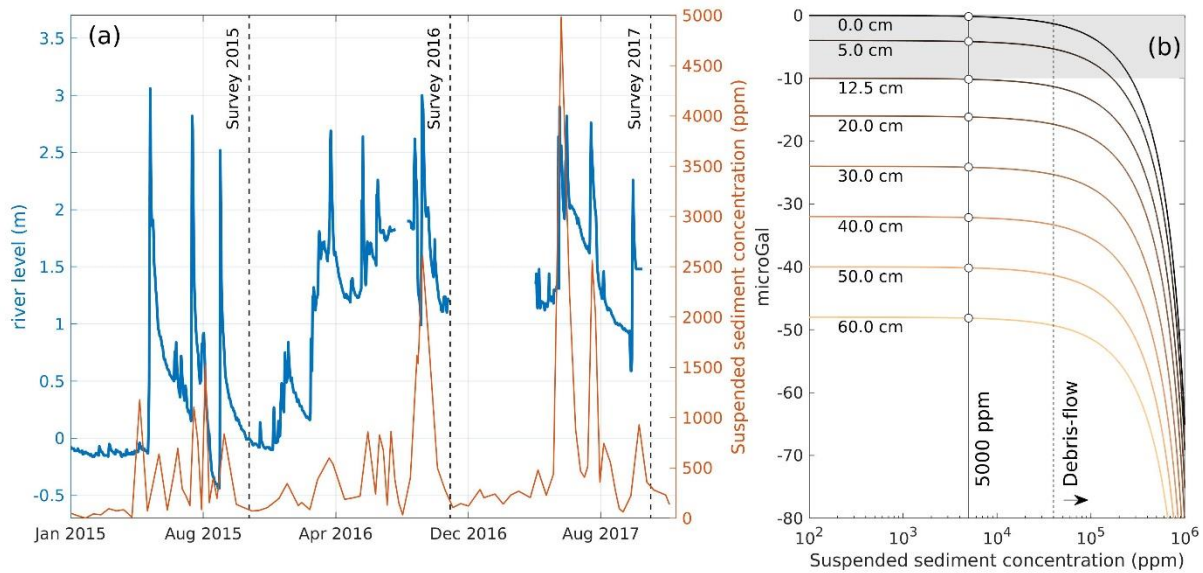
Figure 12: a) River level and sediment concentration of Laonong River, measured at LiuGui station, about 20 km downstream from Paolai. The highest sediment concentration (5000 ppm) is reached in summer 2017, when the river level increased by about 1.6 m.

Data are freely available at the Taiwan WRA (Taiwan Water Resources Agency, 2019)**. b) Estimated gravity changes at the buried network (Fig. 11c) as a function of the variations of the suspended sediment load and of increasing amounts of bedload-transported sediment. The bedload fraction is considered here as a homogenous layer of 0 to 60 cm thickness (labelled on each curve) and density 2×10^3 kg m^{-3}. The river becomes a debris-flow when its suspended sediment concentration goes beyond 4×10^4 ppm. The 5000 ppm level is shown as a reference. Note that the gravity sign is negative because the mass is increased above the gravimeters.**
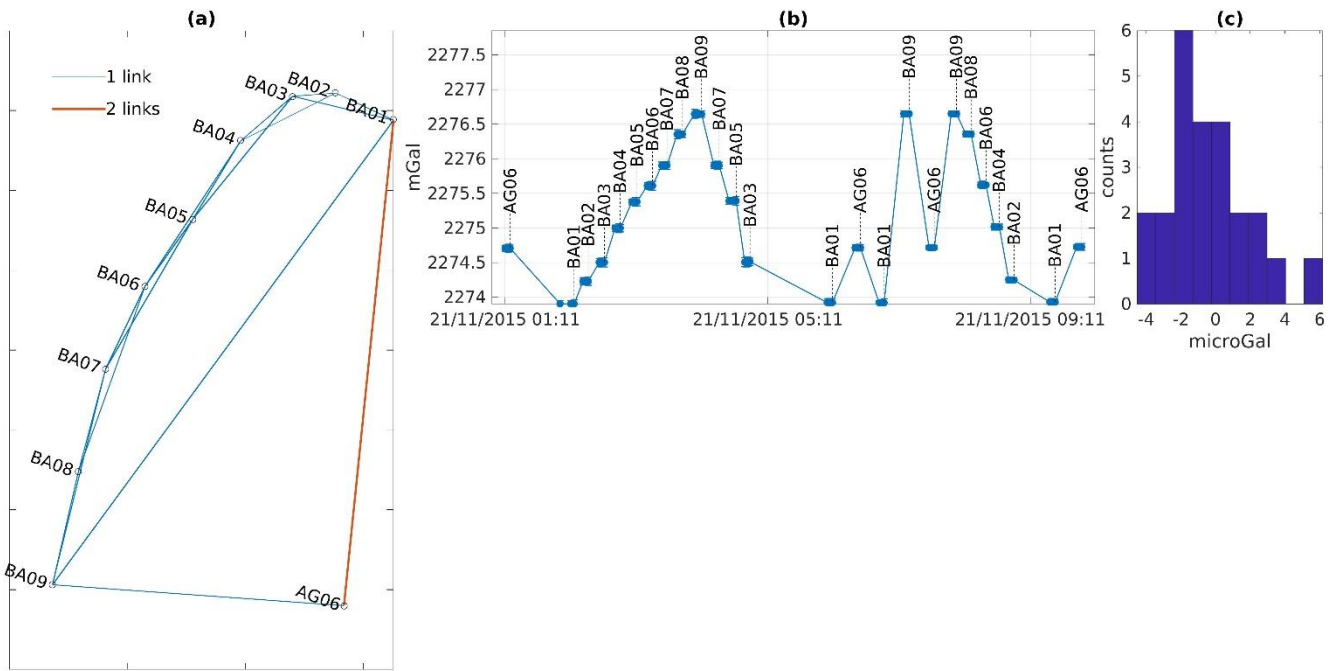
Figure A1: (a) Map view of the relative gravity network with the link between each site for the 2015 survey. (b) Gravity readings on the CG5 at each site as a function of time. (c) Histogram of the residuals after the drift adjustment.

885
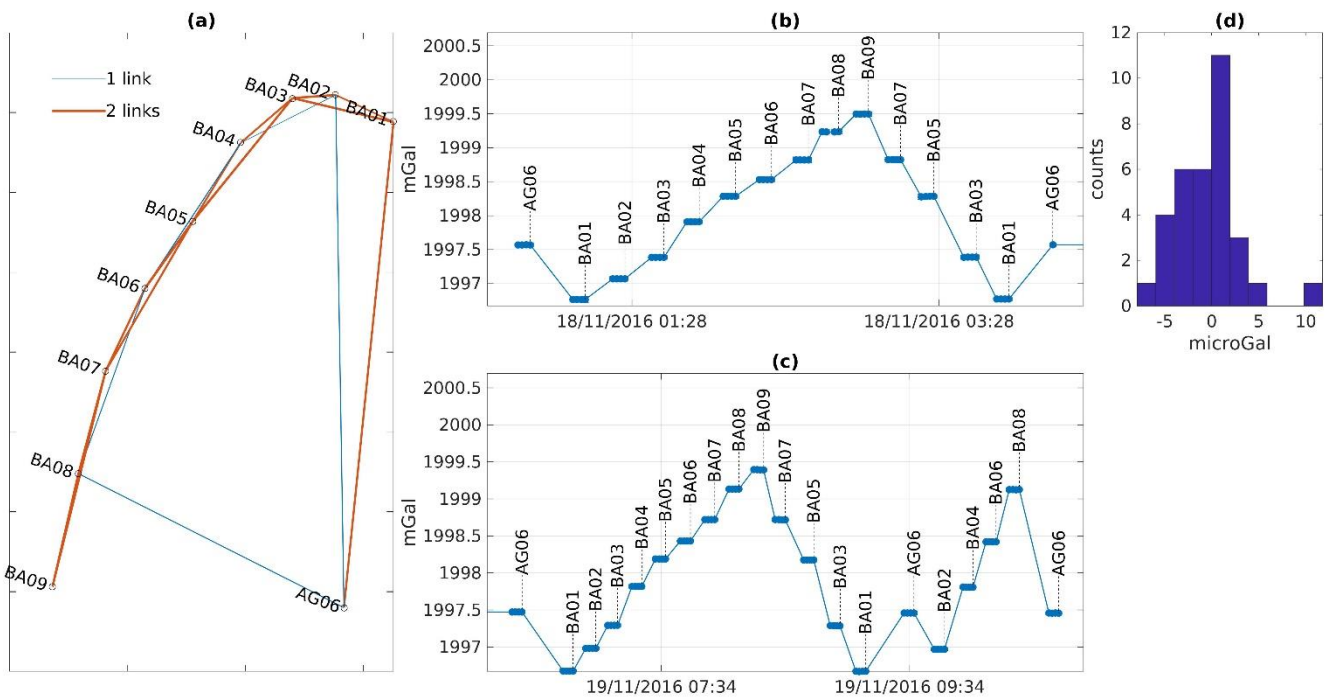
Figure A2: (a) Map view of the relative gravity network with the link between each site for the 2016 survey. (b) and (c) Gravity readings on the CG5 at each site as a function of time. (d) Histogram of the residuals after the drift adjustment.

890
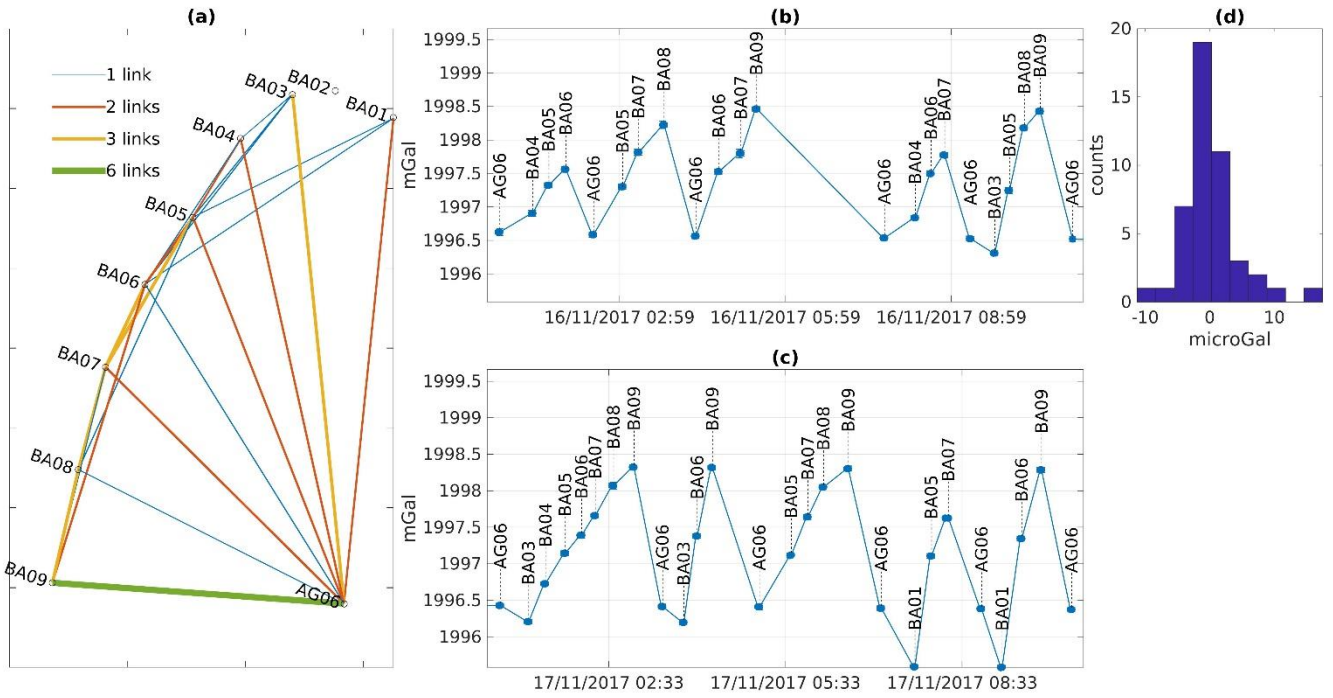
Figure A3: (a) Map view of the relative gravity network with the link between each site for the 2017 survey. (b) and (c) Gravity readings on the CG5 at each site as a function of time. (d) Histogram of the residuals after the drift adjustment.

895
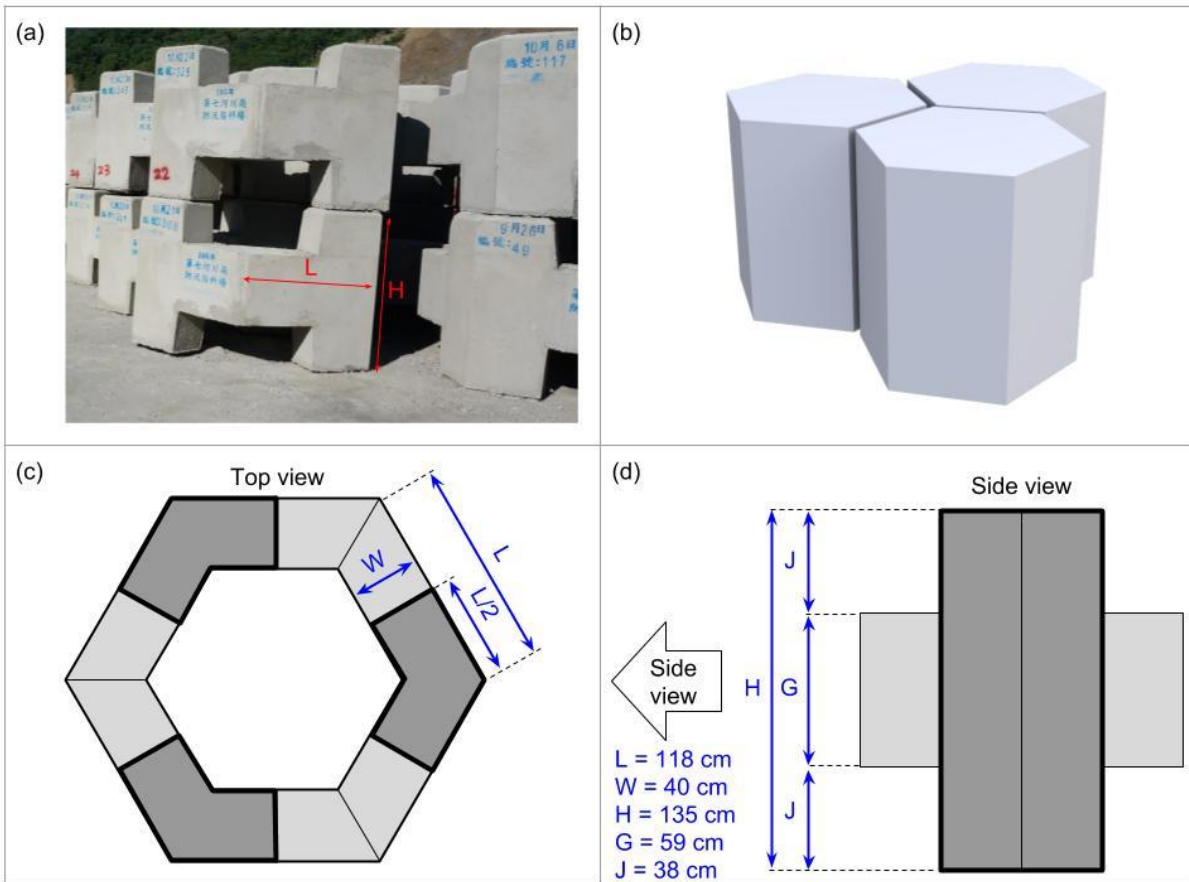
Figure B1: a) Photography of the dolosse. b) 3D hexagonal shape of the plain dolosse, as seen by the photogrammetry. c) Top view of the actual dolosse. The dark gray parts are the pillars actually touching the ground and the light gray parts are the "arms" of the dolosse. d) Side view of one dolosse element. One dolosse consists in three of these parts, joined by the arms.

905
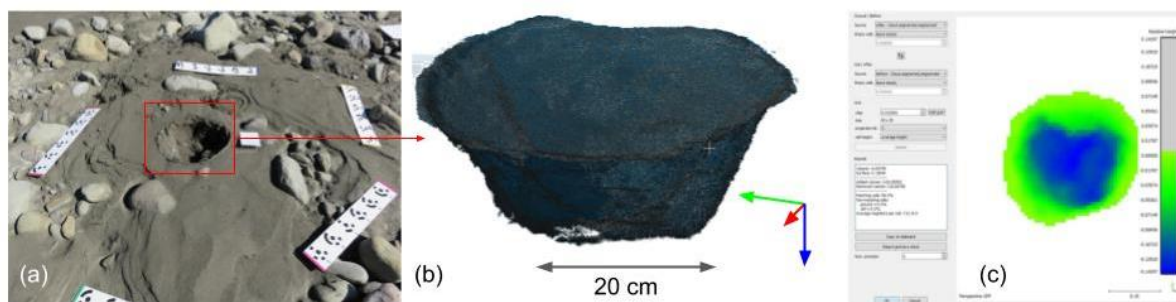
Figure C1: a) Picture of the hole taken with references scales and benchmarks. Several pictures were thus taken before and after the hole was dug. b) 3D cloud of the points mapping the surface of the hole. c) Computation of the volume bounded by the hole and the former surface of the ground, before the hole was done.

910